

# Asymptotic and numerical Green's function in a lined duct with realistic shear and swirl

James Mathews\*, and Nigel Peake†

*University of Cambridge, Cambridge, CB3 0WA, UK*

Stefano Bianchi‡

*Rolls-Royce plc, Derby, DE24 8BJ, UK*

This study considers the asymptotic and numerical Green's function in a lined duct with realistic mean flow. The realistic mean flow will have both shear and swirling components. We will show that the high frequency asymptotic Green's function we derive is a very good approximation for all mean flows, provided the (non-dimensionalised) frequency  $\omega$  is sufficiently large. Generally we will require  $\omega \gtrsim 15$  to be a good approximation to the numerical Green's function. In calculating the Green's function asymptotically, we derived dispersion relations for the asymptotic eigenmodes, although they have to be solved numerically. Once we have accurately modelled the Green's function there are a number of applications, such as beamforming.

## Nomenclature

### Latin Characters

$A_j$	source auto-power in beamforming
$C$	Cross spectral matrix used in beamforming
$\mathcal{C}$	Contour enclosing the critical layer and hydrodynamic modes
$c_0$	Base flow speed of sound
$c_p, c_v$	Specific heat capacities at constant pressure and volume respectively
$D_0/Dt$	Base flow convective derivative
$F$	Transfer function for beamforming
$\mathcal{F}^{PP}, \mathcal{F}^M$	Sixth order differential operators acting on pressure in acoustic analogy
$G_n$	Axial Fourier transform of the $n$ -th azimuthal Fourier series coefficient of $G_\omega$
$G_\omega$	Reduced Green's function at a particular frequency
$\mathbf{g}_j$	Steering vector used in beamforming
$g_1, g_2$	Solutions to the homogeneous equation that $G_n$ solves with certain boundary conditions
$h$	Non-dimensionalised inner radius of the duct
$J$	Jump in derivative when finding the Green's function
$\mathcal{K}_n^+$	Set of all acoustic upstream eigenmodes
$\mathcal{K}_n^-$	Set of all acoustic downstream eigenmodes
$k$	Axial wavenumber and eigenmode
$k_n^j$	A specific acoustic eigenmode indexed by $j$ at a specific azimuthal number $n$
$n$	Azimuthal number
$P$	Fourier transform of pressure perturbation
$\underline{p}$	Total pressure (sum of perturbation and base flow)
$p$	Pressure perturbation
$p_0$	Base flow pressure

---

\*Ph.D student, Department of Applied Mathematics and Theoretical Physics (DAMTP), jrm214@cam.ac.uk. Student member.

†Professor, Department of Applied Mathematics and Theoretical Physics (DAMTP), np100@cam.ac.uk. Senior member.

‡Fan & Compressors Aeroacoustics Specialist, Rolls-Royce, Stefano.Bianchi@rolls-royce.com.

$\hat{p}_n$	Axial Fourier transform of the $n$ -th azimuthal Fourier series coefficient of $\hat{p}_\omega$
$\hat{p}_n^{CL}$	Contribution towards $\hat{p}_n$ from the integral enclosing the critical layer
$\hat{p}_n^j$	Contribution towards $\hat{p}_n$ from the acoustic eigenmode $k_n^j$
$\hat{p}_\omega$	Reduced Green's function at a particular frequency to match Posson and Peake <sup>1</sup>
$q_n$	Function in WKB equation. The number of zeros of $q_n$ determines the form of the solution
$\mathcal{R}, \mathcal{T}$	Differential operators in the acoustic analogy
$r$	Non-dimensionalised radial coordinate
$\mathbf{r}_0 = (x_0, r_0, \theta_0)$	Source position
$r_c$	Zero of $q_n$
$S$	Fourier transform of entropy perturbation
$S_0$	Base flow entropy
$\mathbb{S}_{PP}, \mathbb{S}_M$	Source terms in acoustic analogy
$s^\pm$	Function used to find $\mathcal{K}$ , $\mathcal{K} = s^+(\mathcal{R}) \cup s^-(\mathcal{R})$
$t$	Time
$U, V, W$	Fourier transform of velocity perturbations
$U_\theta(r)$	Swirl profile for base flow
$U_x(r)$	Shear profile for base flow
$\mathcal{U}_\theta$	Function in differential equation for $G_n$ which depends only on swirl $U_\theta$
$\underline{u}, \underline{v}, \underline{w}$	Total velocities (sum of perturbation and base flow)
$u, v, w$	Velocity perturbations
$u_0, v_0, w_0$	Base flow velocities
$\mathcal{V}$	Wronskian of $v_1$ and $v_2$
$v_1, v_2$	Scaled versions of $g_1$ and $g_2$ used in WKB solution
$\mathcal{W}$	Wronskian of $g_1$ and $g_2$
$x$	Non-dimensionalised axial coordinate
$Z_j$	Complex impedance of acoustic lining at duct walls

#### Greek Characters

$\alpha$	If $\alpha > 0$ then $\Re(q_n) > 0$ at $r = 1$ and $\Re(q_n) < 0$ at $r = h$
$\beta$	Varying parameter in base flow entropy $S_0(r) = -\log(r^\beta)$
$\Gamma$	Contour for calculating the inverse Fourier transform on, using the Briggs-Bers method
$\gamma$	Ratio of specific heat capacities
$\delta$	Dirac delta
$\zeta$	Compressibility factor, used in the numerical eigenvalue problem
$\theta$	Circumferential coordinate
$\kappa$	Scaled axial wavenumber, $\kappa = k/\omega$
$\kappa_n^j$	A specific scaled acoustic eigenmode indexed by $j$ at a specific azimuthal number $n$
$\eta$	Scaled azimuthal number, $\eta = n/\omega$
$\xi_j$	Scan points in beamforming
$\rho_0$	Base flow density
$\Sigma_h, \Sigma_1$	Functions relating to the impedance at the duct walls
$\sigma_h, \sigma_1$	Functions relating to the impedance at the duct walls, zero for hard walls
$\tau$	Variable that the Airy functions act on in the WKB solution
$\Upsilon$	Function in differential equation for $G_n$
$\Phi$	Scaled version of $\Omega$ , $\Omega = \omega\Phi$
$\Psi_n$	Integral of $\sqrt{q_n}$ between $r_c$ and 1 used in WKB method for one turning point solution
$\psi_n$	Integral of $\sqrt{q_n}$ in the duct used in WKB method for zero turning point solution
$\bar{\Omega}$	Related function to $\Omega$ , used in the numerical eigenvalue problem
$\Omega$	Function in differential equation for $G_n$ , $\Omega = 0$ defines critical layer
$\Omega_R$	Angular speed of the rotor
$\omega$	Non-dimensionalised frequency

#### Other Characters

$\mathcal{K}$	Region of $\kappa$ space when we should use the one turning point solution in the WKB method
$\mathcal{R}$	Region of $r$ space when we should use the one turning point solution in the WKB method

#### Abbreviations

CAA	Computational aeroacoustics
-----	-----------------------------

CFD	Computational fluid dynamics
WKB	Wentzel-Kramers-Brillouin method <sup>2</sup> for solving a differential equation with a small parameter.

## I. Introduction

In this study we compare the numerical and asymptotic Green’s function for realistic mean flow in a turbofan aeroengine. This realistic mean flow will have both shear and swirl components, which depend only on radial position. We develop a high-frequency asymptotic approximation for the eigenmodes and eigenfunctions for flow in a lined duct, which allows us to calculate the asymptotic Green’s function for the sixth order acoustic analogy derived in Posson and Peake<sup>1</sup> or Mathews.<sup>3</sup>

Recent work on the subject (aside from Mathews<sup>3</sup>) has mainly focused on when we have no swirl or when we have hard walls in the duct. In addition, most of the studies have been numeric. In Wundrow and Khavaran<sup>4</sup> a high-frequency limit is first considered, but in a very simplified case when we have no swirl and are in free space. Free space is much simpler than a lined duct, since we don’t have to consider the critical layer (it doesn’t exist) and our integration contour is just on the real line. In Cooper and Peake<sup>5</sup> and Heaton and Peake<sup>6</sup> WKB analysis is used to construct high-frequency eigenfunctions for the acoustic modes, although they do not proceed to calculate a Green’s function. In both papers they show that we can get turning points in the WKB analysis, which corresponds physically to caustics, with the latter paper using the uniformly-valid Langer solution. Although swirl is considered in both, neither paper considers a lined duct.

In Vilenski and Rienstra<sup>7,8</sup> acoustically lined ducts are considered, but the mean flow has no swirling component. In addition, the authors only seek solutions of the Pridmore–Brown equation and not a Green’s function. Some comparisons are made between numerical and asymptotic eigenmodes, although not many. The asymptotics that they choose to focus on are the trajectories of the eigenmodes as the impedances are varied. In Posson and Peake<sup>1,9</sup> the sixth order acoustic analogy is developed, and the eigenmodes and Green’s function are calculate numerically. Both shear and swirl were considered in a hard-walled duct. An acoustically lined duct was then considered in Posson and Peake,<sup>10</sup> with further numerical results presented, although the boundary conditions were wrongly implemented.

In our study we consider several new factors for the first time. First, we consider the high-frequency WKB limit with lined walls. This leads to extra complexity due to the fact that the axial wavenumber  $k$  is complex, meaning we have to be careful in taking roots and worry about branch cuts. Additionally, we consider for the first time a method to distinguish the regions where we need to use the one turning point solution or the zero turning solution in our WKB equation. This is something not considered in Vilenski and Rienstra.<sup>7</sup> Finally, compared to Posson and Peake<sup>1</sup> we can also use any form of shear and swirl, and are not limited to polynomials. As well as calculating the Green’s function asymptotically, we develop our own tool to calculate the Green’s function numerically which agrees exactly with the results in Posson and Peake.<sup>1</sup> We also consider a base flow with varying entropy, which then has a different acoustic analogy and we consider the effect of entropy on the Green’s function.

This paper is laid out as follows. In Section II we consider the geometry of the duct, the boundary conditions, the swirling base flow and the acoustic analogy that the Green’s function solves. In Section III we discuss how to find the Green’s function, and also explain how we could use the Green’s function we have found. For example we could estimate the source terms in the acoustic analogy, or we could use the Green’s function in beamforming. In Section IV we describe our method to calculate the eigenmodes and Green’s function. We summarise both the asymptotic and numerical methods, with the full details and derivation given in Mathews.<sup>3</sup>

The remaining sections consist of results and comparisons between the asymptotic and numerical Green’s function. In Section V we consider a simple test case where the shear and swirl are simple polynomials. In Section VI we consider the effect of entropy on the Green’s function, and finally in Section VII we consider the Green’s function for realistic mean flow. We consider the effect of boundary layers in CFD data, and consider the mean flow at high and low speed.

## II. The acoustic analogy

### A. Geometry of the duct

Our aeroengine model consists of a infinite duct, with the air flowing between two cylinders. This will be a suitable approximation for considering rotor self-noise and the interaction between the rotor and the stator. We use a cylindrical coordinate system, with  $x$  the axial coordinate,  $r$  the radial coordinate and  $\theta$  the circumferential coordinate, as shown in Figure 1.

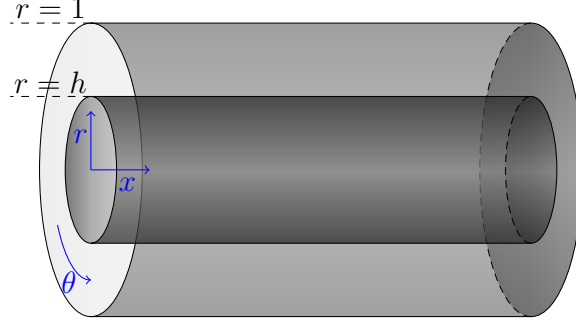


Figure 1: Geometry of the duct.

We let  $\underline{u}$ ,  $\underline{v}$ , and  $\underline{w}$  be the velocities in the  $x$ ,  $r$  and  $\theta$  direction respectively. We non-dimensionalise the duct walls so they lay at  $r = h$  and  $r = 1$ . We split the inviscid total flow into a base flow plus some small perturbation, so we have

$$(\underline{u}, \underline{v}, \underline{w}, \underline{p}) = (u_0, v_0, w_0, p_0) + (u, v, w, p). \quad (1)$$

### B. Lining of the aeroengine and Ingard-Myers boundary condition

In the duct we can either consider the walls to be hard or have an acoustic lining. If we have hard walls then the boundary condition for the flow is very simple, and says that the normal velocity must be zero at the duct walls, or

$$v_0(h) = v_0(1) = v(h) = v(1) = 0, \quad (2)$$

with the conditions on  $v_0$  coming from the inviscid nature of the flow. If instead the duct walls are treated with an acoustic lining then we can mathematically model this lining by introducing the complex specific impedances  $Z_h$  and  $Z_1$  on the duct walls. We further assume that the lining is locally reacting so these impedances are functions of frequency only, and in fact we will assume that these impedances are constant. The boundary conditions for the unsteady flow are the standard Ingard<sup>11</sup>-Myers<sup>12</sup> boundary conditions, which due to the geometry of the duct are given by

$$\begin{aligned} i\omega v &= \left( -i\omega + u_0 \frac{\partial}{\partial x} + v_0 \frac{\partial}{\partial r} + \frac{w_0}{r} \frac{\partial}{\partial \theta} \right) \left( \frac{p}{Z_h} \right) \text{ on } r = h, \\ -i\omega v &= \left( -i\omega + u_0 \frac{\partial}{\partial x} + v_0 \frac{\partial}{\partial r} + \frac{w_0}{r} \frac{\partial}{\partial \theta} \right) \left( \frac{p}{Z_1} \right) \text{ on } r = 1. \end{aligned} \quad (3)$$

These boundary conditions mean we do not have to consider the boundary layer at the duct walls, and we investigate this further in Section VII.A. In the Ingard-Myers boundary condition we have assumed the time dependence of the flow is of the form  $\exp(-i\omega t)$ . The impedances we choose should be of the form  $Z_j = 1 - Zi$ , where  $Z$  is positive, as suggested in Posson and Peake.<sup>10</sup> A typical choice that we will use is  $Z_j = 1 - 2i$ . We consider  $\Re(Z_j) = 1$  a realistic value<sup>10</sup> of impedance after non-dimensionalisation. The case of hard walls corresponds to an impedance of the form  $Z_j = \infty$ , for which the boundary conditions in (3) reduce to (2).

### C. Base flow

The base flow solves the linearised Euler equations. We define it by specifying the base flow velocities, and then we can calculate the pressure, density and speed of sound from the Euler equations. We initially assume

a homentropic flow so the entropy is constant. We choose a base flow of the form

$$(u_0, v_0, w_0) = (U_x(r), 0, U_\theta(r)), \quad (4)$$

where  $U_x$  and  $U_\theta$  are freely chosen. This will give a base flow representative of swirling mean flow in an aeroengine. Numerical CFD calculations suggest that for the swirling flow between the rotor and stator,  $u_0$  and  $w_0$  have a similar amplitude, while the amplitude of  $v_0$  is around 10 – 15% of  $u_0$  and  $w_0$ . Thus, neglecting  $v_0$  should give realistic results. The assumption that the base flow velocity only depends on  $r$  is needed to simplify calculations, but in CFD results the dependence of  $\theta$  and  $x$  is considerably weaker than the dependence on  $r$ . We then find the speed of sound is given by

$$c_0^2(r) = c_0^2(1) + (\gamma - 1) \int_1^r \frac{U_\theta^2(s)}{s} ds, \quad (5)$$

where  $\gamma$  is the ratio of specific heat capacities and  $\gamma = 1.4$  for air. The density is given by

$$\rho_0(r) = [c_0^2(r)]^{1/(\gamma-1)}, \quad (6)$$

and finally the pressure is given by

$$p_0(r) = p_0(1) - \int_r^1 \frac{\rho_0(s) U_\theta^2(s)}{s} ds. \quad (7)$$

#### D. Acoustic analogy from Posson and Peake<sup>1</sup>

In Posson and Peake<sup>1</sup> an acoustic analogy is derived. This analogy was derived by considering an exact rearrangement of the Euler equations, such that we got a single, linear differential equation for pressure on the left-hand side. On the right-hand side is a source term  $\mathbb{S}$  which includes the non-linear effects, viscosity effects and the rotor-stator geometry. The analogy is given by

$$\mathcal{F}^{PP}(p) = \mathbb{S}_{PP}, \quad (8)$$

where the differential operator  $\mathcal{F}^{PP}$  is given by

$$\begin{aligned} \mathcal{F}^{PP} := & \left( \frac{1}{c_0^2} \frac{D_0^2}{Dt^2} - \frac{\partial^2}{\partial x^2} - \frac{1}{r^2} \frac{\partial^2}{\partial \theta^2} \right) \mathcal{R}^2 + \left( \frac{1}{r} \frac{D_0}{Dt} - U'_x \frac{\partial}{\partial x} - \left( \frac{U_\theta}{r^2} + \frac{U'_\theta}{r} \right) \frac{\partial}{\partial \theta} + \frac{D_0}{Dt} \right) \mathcal{R} \mathcal{T} \\ & + \mathcal{R} \frac{D_0}{Dt} \frac{\partial}{\partial r} \mathcal{T} - \frac{D_0}{Dt} \left[ 2U'_x \frac{\partial}{\partial x} \frac{D_0}{Dt} + 2 \left( \frac{U_\theta}{r} \right)' \frac{\partial}{\partial \theta} \frac{D_0}{Dt} + \left( \left( \mathcal{U}_\theta + \frac{U_\theta^2}{r} \right)' \right) \right] \mathcal{T}, \end{aligned} \quad (9)$$

where

$$\mathcal{R} = \frac{D_0^2}{Dt^2} + \mathcal{U}_\theta, \quad \mathcal{T} = -\frac{D_0}{Dt} \frac{\partial}{\partial r} - \frac{2U_\theta}{r^2} \frac{\partial}{\partial \theta} + \frac{U_\theta^2}{rc_0^2} \frac{D_0}{Dt}, \quad \frac{D_0}{Dt} = \frac{\partial}{\partial t} + U_x \frac{\partial}{\partial x} + \frac{U_\theta}{r} \frac{\partial}{\partial \theta}, \quad (10)$$

and

$$\mathcal{U}_\theta(r) = \frac{2U_\theta(r)}{r} \left( \frac{U_\theta(r)}{r} + U'_\theta(r) \right). \quad (11)$$

The source term  $\mathbb{S}_{PP}$  given in Posson and Peake,<sup>1</sup> and consists of the terms on the right hand side of Equation (3.5).

#### E. Acoustic analogy from Mathews<sup>3</sup>

In Mathews<sup>3</sup> a new acoustic analogy is developed, when we allow the entropy to vary. We thus need to consider the energy equation (for an ideal gas) as well as the mass and momentum equations. We now specify the base flows  $U_x(r)$  and  $U_\theta(r)$  as well as the entropy  $\mathcal{S}_0(r)$ . We find that the speed of sound and pressure are given by

$$c_0^2(r) = c_0^2(1) \exp \left( \frac{\mathcal{S}_0(r) - \mathcal{S}_0(1)}{c_p} \right) + (\gamma - 1) \exp \left( \frac{\mathcal{S}_0(r)}{c_p} \right) \int_1^r \exp \left( -\frac{\mathcal{S}_0(s)}{c_p} \right) \frac{U_\theta^2(s)}{s} ds, \quad (12)$$

and

$$\rho_0(r) = \left[ c_0^2(r) \exp \left( -\frac{\mathcal{S}_0(r)}{c_v} \right) \right]^{1/(\gamma-1)}, \quad (13)$$

where  $c_p$  and  $c_v$  are the specific heat capacities. We then find that

$$\mathcal{F}^M(p) = \mathbb{S}_M, \quad (14)$$

with

$$\begin{aligned} \mathcal{F}^M := & \left( \frac{1}{c_0^2} \frac{D_0^2}{Dt^2} - \frac{\partial^2}{\partial x^2} - \frac{1}{r^2} \frac{\partial^2}{\partial \theta^2} \right) \mathcal{R}^2 + \left( \frac{1}{r} \frac{D_0}{Dt} - U'_x \frac{\partial}{\partial x} - \left( \frac{U_\theta}{r^2} + \frac{U'_\theta}{r} \right) \frac{\partial}{\partial \theta} + \left( \frac{U_\theta^2}{rc_0^2} - \frac{\rho'_0}{\rho_0} \right) \frac{D_0}{Dt} \right) \mathcal{R} \mathcal{T} \\ & + \mathcal{R} \frac{D_0}{Dt} \frac{\partial}{\partial r} \mathcal{T} - \frac{D_0}{Dt} \left[ 2U'_x \frac{\partial}{\partial x} \frac{D_0}{Dt} + 2 \left( \frac{U_\theta}{r} \right)' \frac{\partial}{\partial \theta} \frac{D_0}{Dt} + \left( \left( \mathcal{U}_\theta + \frac{U_\theta^2}{r} \left( \frac{\rho'_0}{\rho_0} - \frac{U_\theta^2}{rc_0^2} \right) \right)' \right) \right] \mathcal{T}, \end{aligned} \quad (15)$$

where  $\mathcal{T}$  is unchanged but now

$$\mathcal{R} = \frac{D_0^2}{Dt^2} + \mathcal{U}_\theta + \frac{U_\theta^2}{r} \left( \frac{\rho'_0}{\rho_0} - \frac{U_\theta^2}{rc_0^2} \right). \quad (16)$$

The source term  $\mathbb{S}_M$  is given in Equation (2.2.38) in Mathews.<sup>3</sup> In the case of constant entropy we can calculate that we have

$$\frac{\rho'_0}{\rho_0} = \frac{U_\theta^2}{rc_0^2}, \quad (17)$$

and hence the acoustic analogy reduces to the one from Posson and Peake<sup>1</sup> since  $\mathcal{F}^M = \mathcal{F}^{PP}$ .

### III. Green's function

We want to find the reduced Green's function  $G_\omega(\mathbf{x}|\mathbf{x}_0)$  of (15), which satisfies

$$\mathcal{F}^M (G_\omega(\mathbf{x}|\mathbf{x}_0)e^{-i\omega t}) = \delta(\mathbf{x} - \mathbf{x}_0)e^{-i\omega t} = \delta(x - x_0) \frac{\delta(r - r_0)}{r} \delta(\theta - \theta_0) e^{-i\omega t}. \quad (18)$$

We look for a reduced Green's function of the form

$$G_\omega(\mathbf{x}|\mathbf{x}_0) = \frac{1}{4\pi^2} \sum_{n=-\infty}^{\infty} e^{in(\theta-\theta_0)} \int_{\mathbb{R}} G_n(r|r_0; \omega, k) e^{ik(x-x_0)} dk, \quad (19)$$

where we choose a Fourier series for the circumferential coordinate to ensure it is  $2\pi$  periodic in  $\theta$ . Using standard results<sup>2</sup>  $G_n$  is then given by

$$G_n(r|r_0; \omega, k) = \frac{1}{r_0 \mathcal{W}(r_0, k) J(r_0, k)} \begin{cases} g_1(r_0; k) g_2(r; k) & r \leq r_0 \\ g_2(r_0; k) g_1(r; k) & r > r_0 \end{cases}, \quad (20)$$

where

$$\mathcal{W}(r_0, k) = g_1(r_0; k) g'_2(r_0; k) - g'_1(r_0; k) g_2(r_0; k), \quad (21)$$

is the Wronskian. The functions  $g_1$  and  $g_2$  solve a second order ordinary differential equation given by

$$\begin{aligned} \frac{p_0}{c_0^2 r} (\mathcal{U}_\theta - \Omega^2)^2 \Omega^2 \frac{d}{dr} \left( \frac{rc_0^2}{p_0(\Omega^2 - \mathcal{U}_\theta)} \frac{dg_j}{dr} \right) + \left[ (\mathcal{U}_\theta - \Omega^2)^2 \left( \frac{\Omega^2}{c_0^2} - k^2 - \frac{n^2}{r^2} \right) \right. \\ \left. + \Upsilon(\mathcal{U}_\theta - \Omega^2) \left[ \Upsilon + \Omega \left( \frac{1}{r} - \frac{\rho'_0}{\rho_0} \right) \right] - \Upsilon' \Omega (\Omega^2 - \mathcal{U}_\theta) + \Upsilon [\Omega (\Omega^2 - \mathcal{U}_\theta)]' \right] g_j = 0. \end{aligned} \quad (22)$$

Additionally,  $g_1$  satisfies the boundary condition at  $r = 1$  and  $g_2$  satisfies the boundary condition at  $r = h$ . The functions  $\Omega$  and  $\Upsilon$  are given by

$$\Omega(r, k) = \omega - k U_x(r) - \frac{n U_\theta(r)}{r} \text{ and } \Upsilon(r, k) = \frac{U_\theta^2(r)}{rc_0^2(r)} \Omega(r, k) + \frac{2n U_\theta(r)}{r^2}. \quad (23)$$

The function  $J$  arises from the jump in the derivative of  $g_j$  at  $r = r_0$ , and is given by

$$J(r_0, k) := [\Omega^2(r_0, k) - \mathcal{U}_\theta(r_0)] \Omega^2(r_0, k). \quad (24)$$

## A. Boundary conditions

From the derivation of the acoustic analogy in Posson and Peake<sup>1</sup> or Mathews<sup>3</sup> we have

$$\rho_0 \mathcal{R}(v) = \mathcal{T}(p), \quad (25)$$

when we ignore source terms. The Ingard-Myers boundary conditions in (3) for our chosen base flow then become

$$\begin{aligned} \frac{i\omega \mathcal{T}(p)}{\rho_0} &= \frac{1}{Z_h} \left( -i\omega + U_x \frac{\partial}{\partial x} + \frac{U_\theta}{r} \frac{\partial}{\partial \theta} \right) \mathcal{R}(p) \text{ on } r = h, \\ -\frac{i\omega \mathcal{T}(p)}{\rho_0} &= \frac{1}{Z_1} \left( -i\omega + U_x \frac{\partial}{\partial x} + \frac{U_\theta}{r} \frac{\partial}{\partial \theta} \right) \mathcal{R}(p) \text{ on } r = 1. \end{aligned} \quad (26)$$

Fourier transforming these then gives the boundary condition at  $r = h$  as

$$\frac{\partial g_2}{\partial r}(h) - \left[ \frac{2nU_\theta(h)}{h^2\Omega(h)} + \frac{U_\theta^2(h)}{hc_0^2(h)} \right] g_2(h) + \frac{i\rho_0(h)}{\omega Z_h} [\Omega^2(h) - \mathcal{U}_\theta(h)] g_2(h) = 0, \quad (27)$$

while the boundary condition at  $r = 1$  is

$$\frac{\partial g_1}{\partial r}(1) - \left[ \frac{2nU_\theta(1)}{\Omega(1)} + \frac{U_\theta^2(1)}{c_0^2(1)} \right] g_1(1) - \frac{i\rho_0(1)}{\omega Z_1} [\Omega^2(1) - \mathcal{U}_\theta(1)] g_1(1) = 0. \quad (28)$$

In the limit of  $Z_j \rightarrow \infty$  then we recover the hard wall boundary conditions from Posson and Peake,<sup>1</sup> which are

$$\frac{\partial g_j}{\partial r}(r) - \left[ \frac{2nU_\theta(r)}{r^2\Omega(r)} + \frac{U_\theta^2(r)}{rc_0^2(r)} \right] g_j(r) = 0, \quad (29)$$

for  $j = 1, r = 1$  and  $j = 2, r = h$ .

## B. Using the Green's function

Once we have the Green's function, we can calculate the pressure by using

$$p = \int G_\omega(r, x, \theta | r_0, x_0, \theta_0) \mathbb{S}(r_0, x_0, \theta_0) d\mathbf{x}_0 e^{-i\omega t}. \quad (30)$$

However, using the full form of  $\mathbb{S}$  is out of the question, since it contains non-linear terms that we do not know. Additionally, using the full geometry of the rotor and stator is too hard. In Posson and Peake<sup>1</sup> an approximation to  $\mathbb{S}$  was considered that allows us to calculate  $p$ .

The model of the rotor and stator is given by Figure 2, where we have unwrapped the  $\theta$  coordinate. We model the rotor and stator as infinitely thin plates with zero lean or sweep.

In Posson and Peake<sup>1</sup> all volume source terms were discarded in  $\mathbb{S}$ , and some surface terms were also discarded, since their effect was thought to be small. The final integral for the pressure was given by Equation (6.2) in Posson and Peake.<sup>1</sup> The pressure can then be calculated if we can calculate the pressure jump over the surface of a blade. This can be done analytically, such as in Posson et al.<sup>13</sup> The details are given in Posson and Peake.<sup>1</sup>

Some reproduced plots (from Posson and Peake<sup>9</sup>) of the pressure function using this method are given later in Figure 5.

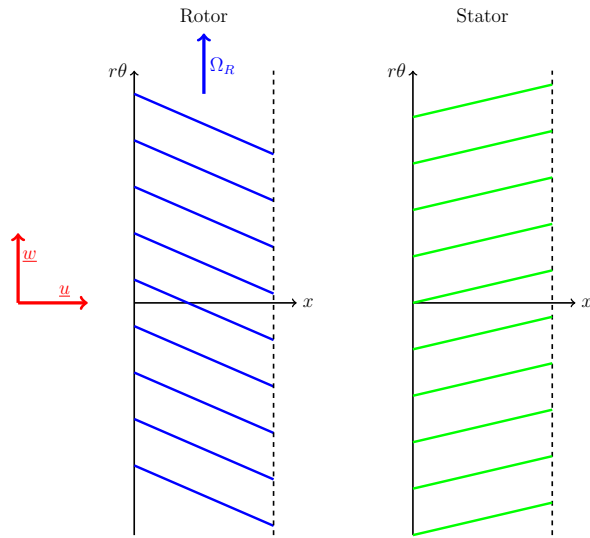


Figure 2: Geometry of the rotor and stator.

### C. Application to beamforming

Beamforming is an imaging technique that has many applications in aeroacoustics and continues to evolve to meet greater challenges. A strong selling point of this technique is the ability of beamforming to locate rogue sources; sources that are not expected and would potentially contaminate the results of conventional aeroacoustics measurements. The beamforming technique is based on knowledge of a propagation model, between sources and unsteady pressure transducers, i.e. the Green's function. Current research on beamforming includes finding ways to accurately represent extended, coherent, source distributions and beamforming in complex, small environments such as turbofan engine nacelles and interstages. Additional research is focussing on expanding the beamforming space to include independent parameters in addition to frequency and spatial coordinates, as well as multipole source distributions.<sup>14, 15</sup> New array designs include multiple sensor modes and methods have been developed to remove effects of turbulent decorrelation,<sup>16</sup> but this remains a big challenge.

The formulation of the classical technique of beamforming in the frequency domain is simple and lends itself to many types of useful analysis. We consider the cross spectral matrix of the array of transducers in Figure 3 with the form:

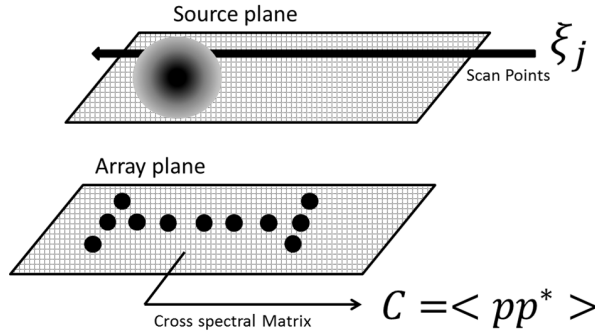


Figure 3: Diagram of beamforming.

$$C = \langle pp^* \rangle. \quad (31)$$

In conventional induct beamforming we estimate the source auto-power  $A_j$  for each scan points  $\xi_j$  by solving

$$\min ||C - A_j \mathbf{g}_j \mathbf{g}_j^*||^2, \quad (32)$$

with  $\mathbf{g}_j$  being the steering vector. The transducers' pressure is assumed due to a theoretical point source in the scan point  $\xi_j$  and the associated solution is

$$A_j = \frac{\mathbf{g}_j^* C \mathbf{g}_j}{(\mathbf{g}_j^* \mathbf{g}_j)^2}. \quad (33)$$

The steering vector can be written in the form

$$\mathbf{g}_j = \begin{pmatrix} g_{1,j} \\ \vdots \\ g_{N,j} \end{pmatrix}, \quad (34)$$

where

$$g_{n,j} = F(\mathbf{x}_n, \xi_j). \quad (35)$$

In this equation  $F$  represents the transfer function in the duct section. If we assume monopole sources only, then  $F$  is a Green's function  $G$  and solves the differential equation

$$LG = -\delta(\mathbf{x}_n - \xi_j) \quad (36)$$

for some operator  $L$ . In case of non-monopole assumption, (e.g. dipole or quadrupole sources)  $F$  is some derivative of the Green's function. The differential equation is solved for the local boundary conditions with  $\mathbf{x}_n$  being the positions of the transducers in the array.



The Green's function is generally known for simple cases such as the radiation in the free and uniform flow, annular duct propagation or rectangular reverberation rooms.<sup>17</sup> To take into account an infinite thin shear layer, Amiet<sup>18</sup> proposed an improved method, largely used by Humphreys,<sup>19</sup> Padois<sup>20</sup> in experimental measurements. Different Green's function models have been also developed assuming only parallel shear flow in the duct.<sup>21</sup> But in realistic industrial problems, the propagation medium properties are largely more complex. In such cases, not using an appropriate Green's function can lead to spurious sources localisation and may create a bias of level estimation. Usage of CAA for the exact calculation of the Green's Function in complex industrial problems has also been demonstrated.<sup>22</sup> Nevertheless the current computational capability of the industry doesn't allow the comfortable usage of numerical techniques in presence of stringent business timescales.

When we perform beamforming in a turbomachinery environment, the Green's function is needed for constructing the steering vectors for in-duct measurements performed in high swirling flow (i.e. the compressor interstage region). Moreover, if wall lining is included, the Green's functions can be used to optimise liners for the different noise sources. In all the above cases the Green's function becomes analytically difficult to determine, due to flow heterogeneity and complex boundary conditions. This happens particularly when the application requires the array to operate over a very wide frequency range, where the classical beamforming gives the best results for incoherent, broadband, source distributions.

For this reason we aim to overcome the above limitations and to implicitly improve the analysis of experimental data in a realistic engine configuration by developing a high-frequency asymptotic approximation for the eigenmodes and eigenfunctions for realistic swirl and shear flow in a lined duct. In spite of this, the method described here can also be applied to sources in unducted sheared flows, e.g., to model sound refraction by the shear layer of a circular open jet of, or to model diffraction and refraction of sound in the presence of a cylindrical fuselage.

#### IV. Method for calculating Green's function

To find the Green's function we first have to find the eigenmodes of the flow. These are particular values of the axial wavenumber  $k$  where we can find a solution  $g^j(r; k)$  which solves (22) and both boundary conditions (27) and (28). Subsequently for these eigenmodes we have  $\mathcal{W}(r_0, k) = 0$ .

In Figure 4 we have a schematic of the eigenmodes for a hard-walled duct. We have also plotted the critical layer, comprising of values of  $k$  for which  $\Omega(r, k) = 0$  for some  $r \in [h, 1]$ . The critical layer corresponds to a mathematical singularity caused by our inviscid assumption.<sup>23</sup> When we have a swirling mean flow, we get hydrodynamic modes accumulating at the edge of the critical layer, with the accumulation rate given in Heaton and Peake.<sup>24</sup> The discrete modes away from the critical layer are the acoustic modes.

Instead of finding  $G_\omega$ , we will find  $\hat{p}_\omega$ , which is defined by

$$\hat{p}_\omega(\mathbf{x}|\mathbf{x}_0) = \frac{1}{4\pi^2} \sum_{n=-\infty}^{\infty} e^{in(\theta-\theta_0)} \int_{\mathbb{R}} \hat{p}_n(r|r_0; \omega, k) e^{ik(x-x_0)} dk, \quad (37)$$

where

$$\hat{p}_n(r|r_0; \omega, k) = \frac{1}{r_0 \mathcal{W}(r_0, k)} \begin{cases} g_1(r_0; k) g_2(r; k) & r \leq r_0 \\ g_2(r_0; k) g_1(r; k) & r > r_0 \end{cases}, \quad (38)$$

so  $\hat{p}_n$  and  $G_n$  differ by a factor of  $J(r_0, k)$ . The pressure would now be given by

$$\frac{D_0^2}{D_t^2} \mathcal{R}(p) = \int \hat{p}_\omega(r, x, \theta|r_0, x_0, \theta_0) \mathbb{S}(r_0, x_0, \theta_0) d\mathbf{x}_0 e^{-i\omega t}. \quad (39)$$

Although this is less useful for calculating the pressure function, it is directly comparable to the Green's function in Posson and Peake<sup>1</sup> and also allows easy comparison with the case of no swirl.

To calculate the inverse Fourier transform of  $\hat{p}_n$  we need to calculate

$$\begin{aligned} & \int_{\mathbb{R}} \hat{p}_n(r|r_0; \omega, k) e^{ik(x-x_0)} dk \\ &= \int_{\Gamma} \frac{1}{r_0 \mathcal{W}(r_0, k)} [g_1(r_0; k) g_2(r; k) \mathbb{1}_{r \leq r_0} + g_2(r_0; k) g_1(r; k) \mathbb{1}_{r > r_0}] e^{ik(x-x_0)} dk. \end{aligned} \quad (40)$$

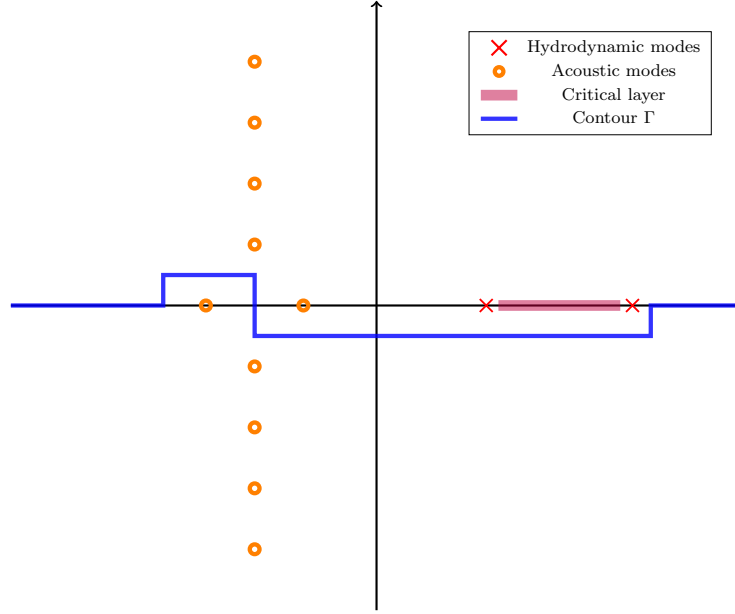


Figure 4: Schematic of eigenmodes and contour of integration for flow in a hard-walled duct.

It is clear that we can no longer integrate over the real line, since we have eigenmodes on the real line, where  $\mathcal{W}(r_0, k) = 0$ . Instead, we choose a contour  $\Gamma$  of the form given in Figure 4. This was chosen by considering the stability of the eigenmodes, using the Briggs-Bers method.<sup>25</sup>

Finally, to perform the integration we close the contour in the upper or lower half plane depending on whether  $x > x_0$ . When  $x > x_0$  we close the contour in the upper half plane, and the Green's function is equal to the sum of the residues at the upstream eigenmodes, plus a critical layer contribution. This is calculated by choosing a contour  $\mathcal{C}$  which encloses the critical layer and the hydrodynamic modes. When  $x < x_0$  we close the contour in the lower half plane, and just get a sum of the residues at the downstream eigenmodes, with no contribution from the critical layer.

#### 1. Contribution from the acoustic eigenmodes

The total contribution from the acoustic eigenmodes is given by

$$\hat{p}_\omega^A(\mathbf{x}|\mathbf{x}_0) = \sum_{n=-\infty}^{\infty} e^{in(\theta-\theta_0)} \sum_{k_n^j \in \mathcal{K}_n^\pm} \hat{p}_n^j, \quad (41)$$

where

$$\hat{p}_n^j(\mathbf{x}|\mathbf{x}_0) = \pm \frac{2\pi i}{4\pi^2} \text{Res}\{\hat{p}_n(r|r_0; \omega, k) e^{ik(x-x_0)}, k = k_n^j\}. \quad (42)$$

The  $\pm$  comes from whether  $x > x_0$  or  $x < x_0$ , with  $\mathcal{K}_n^+$  consisting of all upstream acoustic modes and  $\mathcal{K}_n^-$  consisting of all the downstream acoustic modes. We can calculate that

$$\hat{p}_n^j(\mathbf{x}|\mathbf{x}_0) = \pm \frac{2\pi i}{4\pi^2} \frac{1}{r_0 \frac{\partial \mathcal{W}}{\partial k}(r_0, k_n^j)} e^{ik_n^j(x-x_0)} \begin{cases} g_1(r_0; k_n^j) g_2(r; k_n^j) & r \leq r_0 \\ g_2(r_0; k_n^j) g_1(r; k_n^j) & r > r_0 \end{cases}, \quad (43)$$

and we also note that  $g_1(r; k_n^j) = g_2(r; k_n^j)$ . Acoustic cut-off modes with large imaginary parts will contribute very little to the Green's function due to the exponential term  $\exp(ik(x-x_0))$ . Because of this we only need to consider the first couple of cut-off modes, but all the cut-on modes need to be considered.

## 2. Contribution from the critical layer and hydrodynamic modes

When  $x > x_0$  we need to consider the effect of the critical layer, since we are closing the contour in the upper half plane. The critical layer is calculated using a counter clockwise contour  $\mathcal{C}$  enclosing the critical layer and hydrodynamic modes, and is given by

$$\hat{p}_\omega^{CL}(\mathbf{x}|\mathbf{x}_0) = \sum_{n=-\infty}^{\infty} e^{in(\theta-\theta_0)} \hat{p}_n^{CL}, \quad (44)$$

where

$$\hat{p}_n^{CL}(\mathbf{x}|\mathbf{x}_0) = \frac{1}{4\pi^2} \int_{\mathcal{C}} \hat{p}_n(r|r_0; \omega, k) e^{ik(x-x_0)} dk. \quad (45)$$

We could evaluate the contribution from each hydrodynamic mode separately by using a similar method to that for the acoustic eigenmodes. When  $x < x_0$  then is no contribution from the critical layer.

## 3. Significance of the critical layer

We ignore the contribution from the critical layer, since it is very expensive to compute and generally insignificant compared to the contribution from the acoustic eigenmodes. This was shown in Posson and Peake.<sup>9</sup> In Figure 5 we can see the pressure field due to rotor self-noise, reproduced from Posson and Peake.<sup>9</sup>

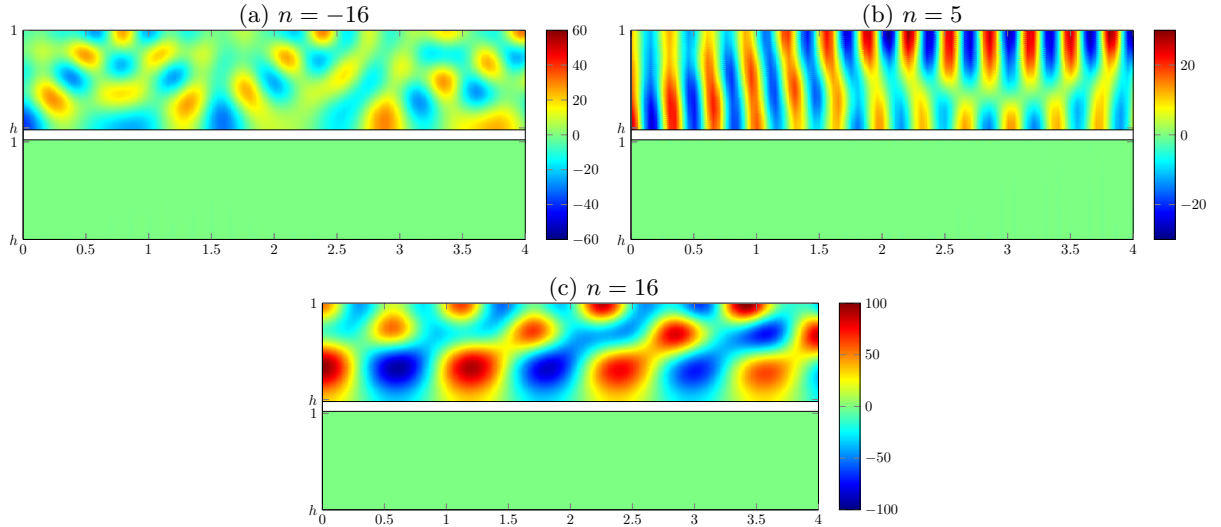


Figure 5: **Comparison of the effect of the acoustic modes and critical layer.** We have reproduced part of Figure 4 from Posson and Peake<sup>9</sup> showing the pressure field. The pressure field is calculated from using the numerical Green's function and a simple model of the rotor. The top colour plot in each subfigure is the contribution from the acoustic modes and the bottom colour plot is the contribution from the critical layer. The parameters are  $\omega = 30$ ,  $h = 0.5$ ,  $U_x = 0.4$  and  $U_\theta(r) = 0.28r$ , hard walls and different values of  $n$ .

It was calculated using a numerical Green's function with a simple rotor model. The top and the bottom plots in each subfigure show the contribution from the acoustic modes and integral around the critical layer respectively. We can see that for these parameters we can ignore the contribution from the critical layer integral for all three values of azimuthal number since it is so much smaller than the contribution from the acoustic modes.

## A. Numerically calculating eigenmodes

To numerically calculate the eigenmodes, we first take the linearised mass, momentum and energy equations, which gives us five equations. We then Fourier transform the variables  $u$ ,  $v$ ,  $w$ ,  $p$  and  $s$  (entropy), with their Fourier transforms given by the respective capital letters. We then solve the resulting eigenvalue problem

for the axial wavenumber  $k$ . The final eigenvalue problem is given by

$$-\frac{U_x \bar{\Omega}}{c_0^2 \zeta} iU + \left[ \frac{U_x}{c_0^2 \zeta} \frac{dU_x}{dr} - \frac{1}{r\zeta} - \frac{U_\theta^2}{\zeta r c_0^2} \right] V - \frac{1}{\zeta} \frac{dV}{dr} - \frac{n}{r\zeta} iW + \frac{i\bar{\Omega}}{c_0^2 \rho_0 \zeta} P = kiU, \quad (46)$$

$$\frac{\bar{\Omega}}{U_x} V - \frac{2U_\theta}{rU_x} iW + \frac{i}{\rho_0 U_x} \frac{dP}{dr} - \frac{iU_\theta^2}{\rho_0 U_x r c_0^2} P + i \frac{U_\theta^2}{r c_p U_x} S = kV, \quad (47)$$

$$-\frac{1}{U_x} \left[ \frac{U_\theta}{r} + \frac{dU_\theta}{dr} \right] V + \frac{\bar{\Omega}}{U_x} iW - \frac{in}{r \rho_0 U_x} P = kiW, \quad (48)$$

$$-\frac{i\rho_0 \bar{\Omega}}{\zeta} iU + i \frac{\rho_0}{\zeta} \left[ \frac{dU_x}{dr} + (\zeta - 2) \frac{U_x}{r} \right] V - \frac{i\rho_0 U_x}{\zeta} \frac{dV}{dr} - \frac{in\rho_0 U_x}{r\zeta} iW - \frac{U_x \bar{\Omega}}{c_0^2 \zeta} P = kP, \quad (49)$$

$$i \frac{1}{U_x} \frac{dS_0}{dr} V + \frac{\bar{\Omega}}{U_x} S = kS, \quad (50)$$

where

$$\bar{\Omega} = \omega - \frac{nU_\theta}{r} \text{ and } \zeta = 1 - \frac{U_x^2}{c_0^2}. \quad (51)$$

The boundary conditions for the eigenvalue problem are given by

$$Z_h \frac{\omega V(h)}{U_x(h)} + \frac{\bar{\Omega}(h)P(h)}{U_x(h)} - kP(h) = 0, \quad (52)$$

and

$$Z_1 \frac{\omega V(1)}{U_x(1)} - \frac{\bar{\Omega}(1)P(1)}{U_x(1)} + kP(1) = 0. \quad (53)$$

The derivation is given in Mathews.<sup>3</sup> We have solved this eigenvalue problem using Chebfun in MATLAB, which avoids having to discretise the derivatives. We find that we get perfect agreement in all cases with Posson and Peake<sup>1</sup> once we have corrected a numerical implementation error in the boundary condition in Posson and Peake<sup>1</sup> when we have lining.

## B. Numerically calculating Green's function

Once we have calculated the eigenmodes (and eigenfunctions) for the Green's function the only remaining difficulty is calculating the derivative of the Wronskian with respect to  $k$ . The method used to do this is given in both Posson and Peake<sup>1</sup> and Mathews.<sup>3</sup> Essentially, it involves differentiating (22) with respect to  $k$  and getting a differential equation for  $dg_j/dk$ , but with non-zero right hand side. From this we are able to calculate the derivative of the Wronskian. We tested our numerical Green's function with that from Posson and Peake,<sup>1</sup> and got perfect agreement for hard walls.

## C. Asymptotically calculating eigenmodes

The differential equation in (22) is too complicated to solve analytically, so we will consider the equation in the high frequency limit. This allows us to use WKB analysis to solve the differential equation. We summarise the key steps below, with the full details given in Mathews.<sup>3</sup> We introduce the scaling of the axial wavenumber and azimuthal number with frequency:

$$\kappa = \frac{k}{\omega} \text{ and } \eta = \frac{n}{\omega}, \quad (54)$$

and assume that both  $\kappa, \eta = \mathcal{O}(1)$ . Treating  $\omega$  as a large parameter, our differential equation then reduces to

$$\frac{d^2 g_n^j}{dr^2}(r; \kappa) + \left( \frac{1}{r} - \frac{\rho_0'(r)}{\rho_0(r)} - 2 \frac{\frac{\partial}{\partial r} \Phi(r, \kappa)}{\Phi(r, \kappa)} \right) \frac{dg_n^j}{dr}(r; \kappa) + \omega^2 q_n(r, \kappa) g_n^j(r; \kappa) = 0, \quad (55)$$

where

$$\Phi(r, \kappa) = 1 - \kappa U_x(r) - \frac{\eta U_\theta}{r}, \quad (56)$$

and

$$q_n(r, \kappa) := \left( \frac{\Phi^2(r, \kappa)}{c_0^2(r)} - \kappa^2 - \frac{\eta^2}{r^2} \right). \quad (57)$$

However, this high-frequency limit is only valid away from the critical layer since we assume terms of the form  $\Omega = \omega\Phi$  are large. Thus, we can only use it to find acoustic eigenmodes. We can write

$$g_j(r; \kappa) = \frac{\rho_0^{1/2}(r)\Phi(r, \kappa)v_j(r; \kappa)}{r^{1/2}}, \quad (58)$$

and then in the high-frequency limit

$$\frac{d^2 v_j}{dr^2}(r; \kappa) + \omega^2 q_n(r, \kappa)v_j(r; \kappa) = 0. \quad (59)$$

The Green's function is then given by

$$G_n(r|r_0; \kappa) = \left( \frac{\rho_0(r)r_0}{\rho_0(r_0)r} \right)^{1/2} \frac{\Phi(r, \kappa)}{r_0 \mathcal{V}(r_0, \kappa) J(r_0, \kappa) \Phi(r_0, \kappa)} \begin{cases} v_1(r_0; \kappa)v_2(r; \kappa) & r \leq r_0 \\ v_2(r_0; \kappa)v_1(r; \kappa) & r > r_0 \end{cases}, \quad (60)$$

where  $\mathcal{V}$  is the Wronskian of  $v_1(r; \kappa)$  and  $v_2(r; \kappa)$ . By multiplying  $G_n(r|r_0; \kappa)$  by  $J(r_0, \kappa)$  we can get the equation for  $\hat{p}_n(r|r_0; \kappa)$ . We can solve for  $v_j(r; \kappa)$  in (59) using WKB analysis, and we find there are different forms of the solution, depending on how many zeros  $q_n(r, \kappa)$  has in the duct  $[h, 1]$  or close to it. We find that assuming  $q_n(r, \kappa)$  has one or no zeros covers most cases with polynomial shear or swirl. However, we find for some of the realistic mean flow profiles it is quite common to get two (or more) zeros of  $q_n(r, \kappa)$  close to the duct.

When  $q_n(r, \kappa)$  has no zeros then  $v_j(r; \kappa)$  is a linear combination of exponentials, given by

$$v_j(r; \kappa) = |q_n(r, \kappa)|^{-1/4} \left( A^j(\kappa) e^{i\omega\psi_n(r, \kappa)} + B^j(\kappa) e^{-i\omega\psi_n(r, \kappa)} \right) \text{ with } \psi_n(r, \kappa) = \int_h^r \sqrt{q_n(s, \kappa)} ds, \quad (61)$$

for some constants  $A^j$  and  $B^j$ . If  $q_n(r, \kappa)$  has a single zero (at  $r_c$ ) we can use the uniformly-valid Langer solution<sup>6,2</sup> and then

$$v_j(r; \kappa) = \sqrt{\pi} \left( \frac{\tau(r, \kappa)}{q_n(r, \kappa)} \right)^{1/4} \left[ A^j(\kappa) \text{Ai}(-\tau(r, \kappa)) + B^j(\kappa) \text{Bi}(-\tau(r, \kappa)) \right], \quad (62)$$

where

$$\tau(r, \kappa) = \left( \frac{3k\Psi_n(r, \kappa)}{2} \right)^{2/3} \text{ and } \Psi_n(r, \kappa) = \int_{r_c}^r \sqrt{q_n(s, \kappa)} ds. \quad (63)$$

We then apply the boundary conditions to determine the constants  $A^j$  and  $B^j$  of  $v_j(r; \kappa)$ . The eigenmodes are then calculated by solving the dispersion relation  $\mathcal{V} = v_1 v_2' - v_1' v_2 = 0$ , which is independent of  $r$  by Abel's theorem.

### 1. Regions of $\kappa$ space

Let us define

$$\mathcal{R} = \left\{ r \in \mathbb{C} \mid |r - s| < \omega^{-5/6} \text{ for } s \in [h, 1] \right\}, \quad (64)$$

which is the region of  $r$ -space where we have a critical point close to the duct. It is asymptotically defined from the classical WKB one-turning point solution.<sup>2</sup> We then define

$$s^\pm(r_c) = \frac{U_x(r_c) \left( 1 - \frac{\eta U_\theta(r_c)}{r_c} \right) \pm c_0(r_c) \sqrt{\left( 1 - \frac{\eta U_\theta(r_c)}{r_c} \right)^2 + \frac{\eta^2}{r_c^2} [U_x^2(r_c) - c_0^2(r_c)]}}{U_x^2(r_c) - c_0^2(r_c)}, \quad (65)$$

which comes from solving  $q_n(r, \kappa) = 0$  as a quadratic in  $\kappa$ . Finally, let

$$\mathcal{K} = s^+(\mathcal{R}) \cup s^-(\mathcal{R}) = \{s^+(r) | r \in \mathcal{R}\} \cup \{s^-(r) | r \in \mathcal{R}\}. \quad (66)$$

For  $\kappa \in \mathcal{K}$  we have a critical point close to the duct and should use the Langer solution in (62). If  $\kappa \in \mathcal{K}^C$  then we don't have a critical point close to the duct and we should use the exponential solution in (61).

## 2. Zero turning point dispersion relation

If  $\kappa \in \mathcal{K}^C$  then  $q_n(r, \kappa)$  has no zeros close to the duct and we find that

$$v_1(r; \kappa) = A^1(\kappa) |q_n(r, \kappa)|^{-1/4} \left( e^{i\omega\psi_n(r, \kappa)} + e^{2i\omega\psi_n(1, \kappa)} \frac{1 - \sigma_1(\kappa)}{1 + \sigma_1(\kappa)} e^{-i\omega\psi_n(r, \kappa)} \right), \quad (67)$$

$$v_2(r; \kappa) = A^2(\kappa) |q_n(r, \kappa)|^{-1/4} \left( e^{i\omega\psi_n(r, \kappa)} + \frac{1 + \sigma_h(\kappa)}{1 - \sigma_h(\kappa)} e^{-i\omega\psi_n(r, \kappa)} \right), \quad (68)$$

and

$$\mathcal{V}(\kappa) = 2i\omega A^1(\kappa) A^2(\kappa) \frac{1 - \sigma_1(\kappa)}{1 + \sigma_1(\kappa)} \left[ e^{2i\omega\psi_n(1, \kappa)} - \frac{(1 + \sigma_1(\kappa))(1 + \sigma_h(\kappa))}{(1 - \sigma_1(\kappa))(1 - \sigma_h(\kappa))} \right], \quad (69)$$

where

$$\sigma_h(\kappa) = \frac{\rho_0(h)\Phi^2(h, \kappa)}{Z_h \sqrt{q_n(h, \kappa)}} \text{ and } \sigma_1(\kappa) = \frac{\rho_0(1)\Phi^2(1, \kappa)}{Z_1 \sqrt{q_n(1, \kappa)}}. \quad (70)$$

The constants  $A^1$  and  $A^2$  factor out in the Green's function. The dispersion relation is given by

$$e^{2i\omega\psi_n(1, \kappa)} - \frac{(1 + \sigma_1(\kappa))(1 + \sigma_h(\kappa))}{(1 - \sigma_1(\kappa))(1 - \sigma_h(\kappa))} = 0. \quad (71)$$

## 3. One turning point dispersion relation

If  $\kappa \in \mathcal{K}$  then  $q_n(r, \kappa)$  has a single zero  $r_c$  close to the duct and we find

$$v_1(r; \kappa) = \sqrt{\pi} A^1(\kappa) \left( \frac{\tau(r, \kappa)}{q_n(r, \kappa)} \right)^{1/4} \left[ e^{i\pi/4} (1 - i\Sigma_1(\kappa)) \text{Ai}(-\tau(r, \kappa)) + e^{-i\pi/4} (1 + i\Sigma_1(\kappa)) \text{Bi}(-\tau(r, \kappa)) \right], \quad (72)$$

$$v_2(r; \kappa) = \sqrt{\pi} B^2(\kappa) \left( \frac{\tau(r, \kappa)}{q_n(r, \kappa)} \right)^{1/4} [2\Sigma_h(\kappa) \text{Ai}(-\tau(r, \kappa)) + \text{Bi}(-\tau(r, \kappa))], \quad (73)$$

and

$$\mathcal{V}(\kappa) = i\omega A^1(\kappa) B^2(\kappa) e^{-i\pi/4} [\Sigma_1(\kappa)(2\Sigma_h(\kappa) + i) - (2i\Sigma_h(\kappa) + 1)], \quad (74)$$

where

$$\Sigma_h(\kappa) = e^{2i\omega\psi_n(h, \kappa)} \frac{1 + \sigma_h(\kappa)}{1 - \sigma_h(\kappa)} \text{ and } \Sigma_1(\kappa) = e^{2i\omega\psi_n(1, \kappa)} \frac{1 - \sigma_1(\kappa)}{1 + \sigma_1(\kappa)}. \quad (75)$$

This result only holds when

$$\Re(\alpha(\kappa)) := \Re \left( \frac{\partial q_n}{\partial r}(r_c(\kappa), \kappa) \right) > 0, \quad (76)$$

which corresponds to  $\Re(q_n(1, \kappa)) > 0$  and  $\Re(q_n(h, \kappa)) < 0$ . When  $\Re(\alpha(\kappa)) < 0$  we get a similar but different dispersion relation, which is given in Mathews.<sup>3</sup>

## D. Asymptotically calculating Green's function

Using the change of variables in (54) and (58) we find that the contribution from each acoustic mode is given by

$$\hat{p}_n^j(\mathbf{x}|\mathbf{x}_0) = \pm \frac{2\pi i\omega}{4\pi^2} e^{i\omega\kappa_n^j(x-x_0)} \left( \frac{\rho_0(r)r_0}{\rho_0(r_0)r} \right)^{1/2} \frac{\Phi(r, \kappa_n^j)}{r_0 \frac{\partial \mathcal{V}}{\partial \kappa}(r_0, \kappa_n^j) \Phi(r_0, \kappa_n^j)} \begin{cases} v_1(r_0; \kappa_n^j) v_2(r; \kappa_n^j) & r \leq r_0 \\ v_2(r_0; \kappa_n^j) v_1(r; \kappa_n^j) & r > r_0 \end{cases}, \quad (77)$$

where we have already calculated  $v_1$ ,  $v_2$  and  $\mathcal{V}$ . We can easily calculate the derivative of the Wronskian  $\mathcal{V}$  with respect to  $\kappa$ , where  $\mathcal{V}$  is given by (69) or (74). The only other thing to be careful of is making sure we correctly choose the branch cuts for the non-integer roots we need to take to calculate  $v_1$  and  $v_2$ .

## V. A simple test case

We consider the simple test case with  $U_x = 0.5$ ,  $U_\theta(r) = 0.1r + 0.1/r$ ,  $\omega = 25$ ,  $n = 15$  and both hard and lined walls of impedance  $Z_j = 1 - 2i$ . We calculate the eigenmodes and Green's function both numerically and asymptotically. To get the total Green's function we would sum over all azimuthal numbers  $n$ . This test case corresponds to Examples 3 & 4 from Mathews.<sup>3</sup>

### A. Eigenmode results

We give all eigenmodes to two decimal places, and Table 1 provides a legend for the eigenmodes figures, such as Figure 6. We label the cut-off eigenmodes outwards from the real axis. In some cases we get more accurate results using the zero turning point dispersion relation in the region  $\mathcal{K}$ , when we should be using the one turning point dispersion relation. These asymptotic modes are in bold, and there are two reasons for using the “wrong” dispersion relation. First, the region  $\mathcal{K}$  is only asymptotically defined. Secondly, we have assumed that  $v_1$  and  $v_2$  are exponential or sinusoidal at the duct walls when we calculated  $A^j$  and  $B^j$ , when they may in fact just be Airy. In Figure 6 we plot the eigenmodes for the simple test case with both hard and lined walls.









Symbol	Meaning
	The region $\omega\mathcal{K}$ .
	$\kappa$ corresponding to $r_c(\kappa) \in [h, 1]$ .
 or 	Numerical eigenmode.
 or 	Asymptotic eigenmode using the zero turning point dispersion relation (71).
 or 	Asymptotic eigenmode using the one turning point dispersion relations (74).
<b>-6.00 + 2.55i</b>	Eigenmode in $\mathcal{K}$ but we have used the zero turning point dispersion relation.

Table 1: Legend for eigenmode figures.

#### 1. Hard walls

We see that we are able to find each and every asymptotic eigenmode, and our results look very good. We find there are four cut-on modes with imaginary part zero, and the rest of the modes are cut-off. In the case  $U_\theta = 0$  (Example 1 in Mathews<sup>3</sup>) we had six cut-on modes, so the addition of swirl has seen us lose one upstream and one downstream cut-on mode. The four cut-on modes all correspond to a critical radius  $r_c \in [h, 1]$  and are well approximated by solving the one turning point dispersion relation in (74).

The cut-off modes are all symmetric, and are very well approximated. For the first cut-off mode we solve the one turning point dispersion relation, but the rest of them lie outside the region  $\mathcal{K}$  and we can solve the zero turning point dispersion relation in (71) to calculate these. The relative error for the first cut-off mode is 0.77%, while the second one is less accurate with an error of 1.22%. This is because it lies right on the edge of the  $\mathcal{K}$  region. Subsequent cut-off modes become more and more accurate, with the sixth one having a relative error of just 0.03%.

#### 2. Lined duct

We see that the effect of lining shifts the cut-on modes off the real axis and they now have a small imaginary part, which is positive for upstream modes and negative for downstream modes. In addition, the lining breaks the symmetry of the cut-off modes and in this case shifts them all to the right. Finally, the lining has shifted the cut-off eigenmodes further away from the real line.

We find that the asymptotic cut-on modes are as accurate as when we had no lining, while the cut-off modes are slightly less accurate, in particular the first and second cut-off modes. This is because the first cut-off mode is quite close to the edge of the (asymptotically defined)  $\mathcal{K}$  region. We find it is more accurate for this mode to solve the zero turning point dispersion relation than the one turning point dispersion relation. For the rest of the cut-off modes we also solve the zero turning point dispersion relation.

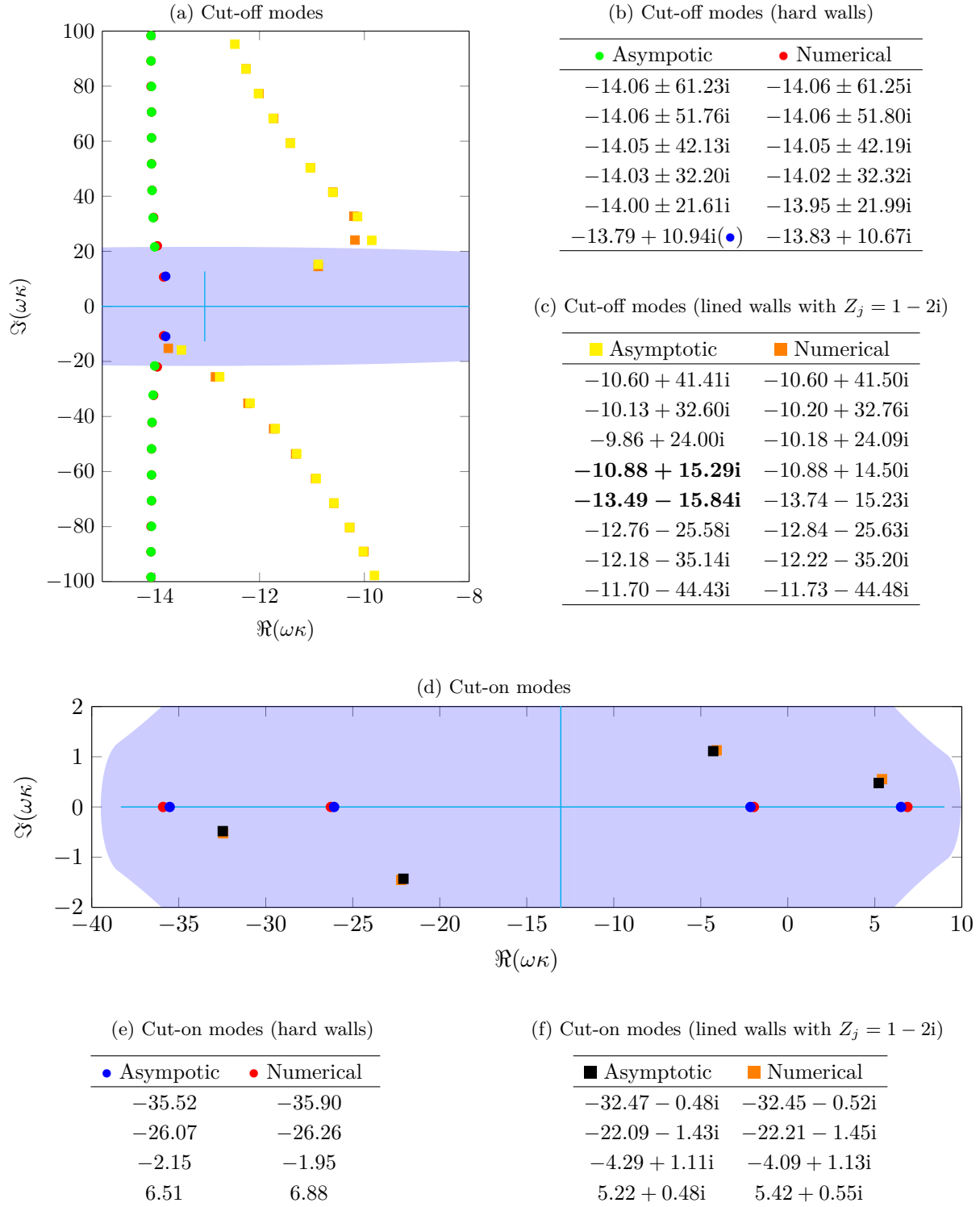


Figure 6: **A simple test case: constant shear with polynomial swirl.**  
Plot of the asymptotic and numerical eigenmodes. The parameters were  $\omega = 25$ ,  $\eta = 0.6$ ,  $U_x = 0.5$ ,  
 $U_\theta(r) = 0.1r + 0.1/r$  with both hard walls and lined walls of impedance  $Z_j = 1 - 2i$ .



## B. Green's function

We now calculate the Green's function contribution,  $\hat{p}_n^i$ , for each cut-on acoustic mode  $k_n^j$  and some of the cut-off modes by using (77). We then sum these contributions to get the Green's function  $\hat{p}_n$ . We generally need to consider at most one or two cut-off modes, since the magnitude of the cut-off modes far away from the real line is very small due to the  $\exp(ik(x - x_0))$  term. However if  $x - x_0$  is very small we might need to consider additional cut-off modes.

We compare both the asymptotic and numerical Green's function for each mode. We will see that the asymptotics provides a very good approximation to the numerical results. We find that in general the closer the asymptotic mode to the numerical mode then the more accurate the asymptotic Green's function is.

We will also show the contribution of the critical layer in the case of hard walls by using (45) and integrating either the numerical form of  $\hat{p}_n$  or the asymptotic form. The integration using the numerical form of  $\hat{p}_n$  is calculated using the solver from Posson and Peake,<sup>1</sup> which is only valid when we have no lining.

### 1. Hard walls

We consider  $x > x_0$ , so we are only interested in the upstream modes. We have set the source to be at  $r_0 = 0.8$  and  $x - x_0 = 0.5$ . There are two upstream cut-on modes and we can see the contribution from them to the Green's function in Figures 7a and 7b. We can see the asymptotic Green's function accurately approximates the numerical Green's function for these cut-on modes. We can see that the contribution from the eigenmode  $k = -2.15$  dominates the contribution from the other cut-on mode.

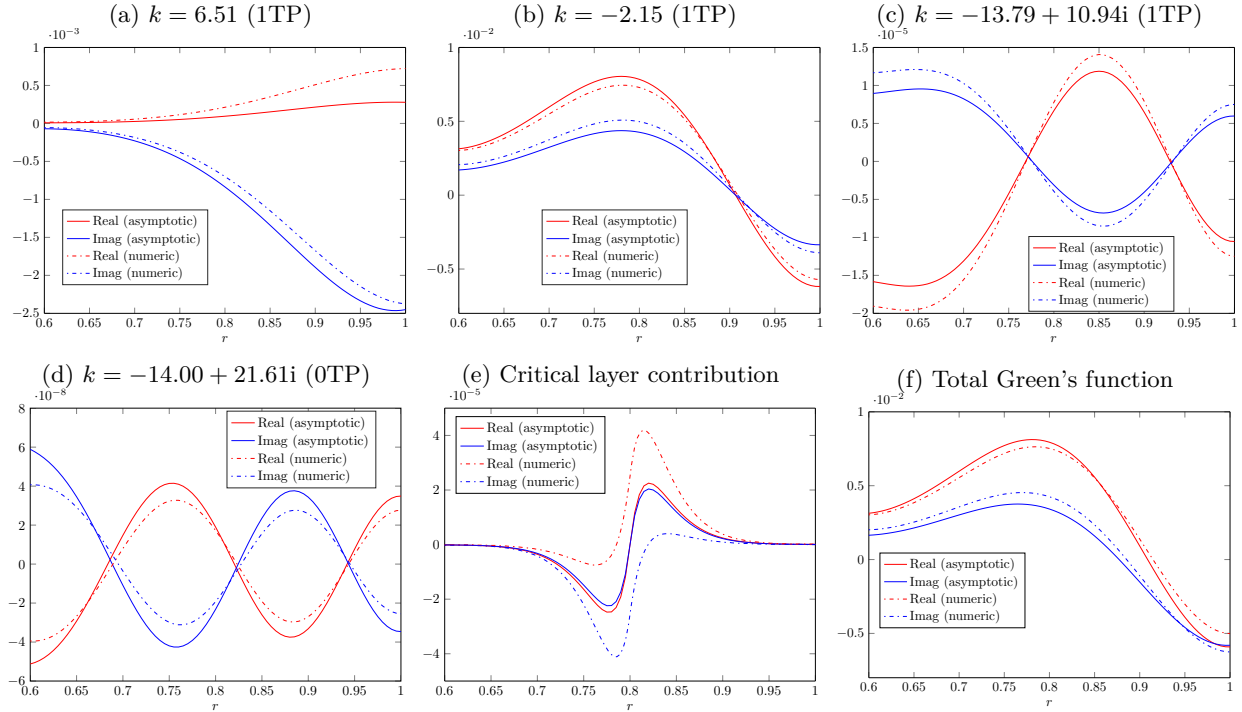


Figure 7: Comparison of the asymptotic and numerical Green's function for the simple test case in a hard-walled duct. We have set the source to be at  $r_0 = 0.8$  and  $x - x_0 = 0.5$ .

The Green's function associated to the first cut-off mode in Figure 7c is several orders of magnitude smaller than the cut-on modes, but still approximates the numerical Green's function well. In Figure 7d we plot the contribution to the Green's function from the second cut-off mode, which is even smaller in magnitude but very well approximated asymptotically. In Figure 7e we see the contribution of the critical layer asymptotically and numerically. We can see that the asymptotic contribution is of a similar order of magnitude to the numerical contribution, although quite a different shape. The reasons for this are discussed in Mathews,<sup>3</sup> but essentially the main reason is that our high-frequency limit is not valid near the critical layer. We can see that the contribution from the critical layer is several orders of magnitude smaller than the cut-on modes, and of a similar magnitude to the first cut-off mode.

Finally, in Figure 7f we see the sum of the contributions from Figures 7a to 7e. The Green's function in this case can be attributed almost entirely to the single eigenmode  $k = -2.15$ .

## 2. Lined duct

We now consider the case of a lined duct. We can see that the asymptotic contribution from the cut-on modes in Figures 8a and 8b accurately approximates the numerical Green's function. Furthermore, the cut-on mode  $k = -4.29 + 1.11i$  dominates the total Green's function. This mode is the transformation of the dominant mode in Figure 7 when we introduce lining.

In Figure 8c we plot the contribution to the Green's function from the first cut-off mode. We have used the asymptotic eigenmode satisfying the zero turning point dispersion relation despite  $\kappa \in \mathcal{K}$ , and this is what causes the inaccuracy in the asymptotic Green's function. However, using the one turning point dispersion relation is actually worse. As mentioned before, this was because we assumed  $v_1$  and  $v_2$  are exponential or sinusoidal at the duct walls when we calculated  $A^j$  and  $B^j$ . In Mathews<sup>3</sup> a more accurate dispersion relation is discussed which gives a more accurate eigenmode and hence Green's function. Nevertheless, the Green's function in Figure 8c is several orders of magnitude smaller than the contribution from the cut-on modes, so this inaccuracy doesn't have much of an effect.

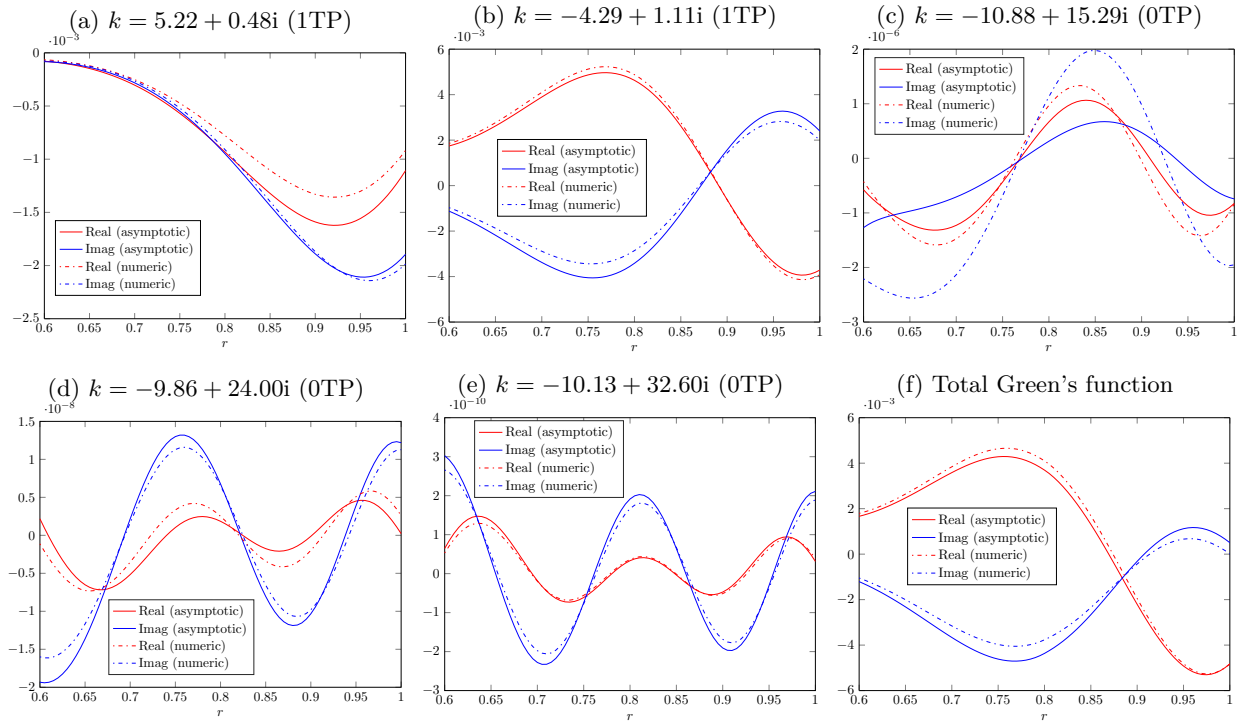


Figure 8: Comparison of the asymptotic and numerical Green's function for the simple test case in a lined duct with walls of impedance  $Z_j = 1 - 2i$ . We have set the source to be at  $r_0 = 0.8$  and  $x - x_0 = 0.5$ .

In Figures 8d and 8e we have plotted the contribution from the Green's function from the second and third cut-off modes. The second cut-off mode is not approximated very well asymptotically but the asymptotic Green's function is still quite accurate. The asymptotic Green's functions from the third cut-off mode is also very accurate. The magnitude of these Green's functions are  $\mathcal{O}(10^{-8})$  and  $\mathcal{O}(10^{-10})$ , so five and seven orders of magnitude smaller than the cut-on modes contribution. In Figure 8f we plot the total Green's function.

## 3. Colour plot of Green's function

Finally, we consider the Green's function for a fixed source  $(x_0, r_0) = (0, 0.8)$  and let both  $x$  and  $r$  vary. In Figure 9 we have colour plots of the real and imaginary parts of the asymptotic Green's function for the simple test cases with hard walls (Figures 9a and 9b) and with lining (Figures 9c and 9d). In a hard-walled duct our Green's function infinitely repeats, while in a lined duct the Green's function decays in the axial

direction. Additionally, the axial periodic changes significantly after the introduction of lining, while the magnitude of the Green's function is smaller when we are in a lined duct.

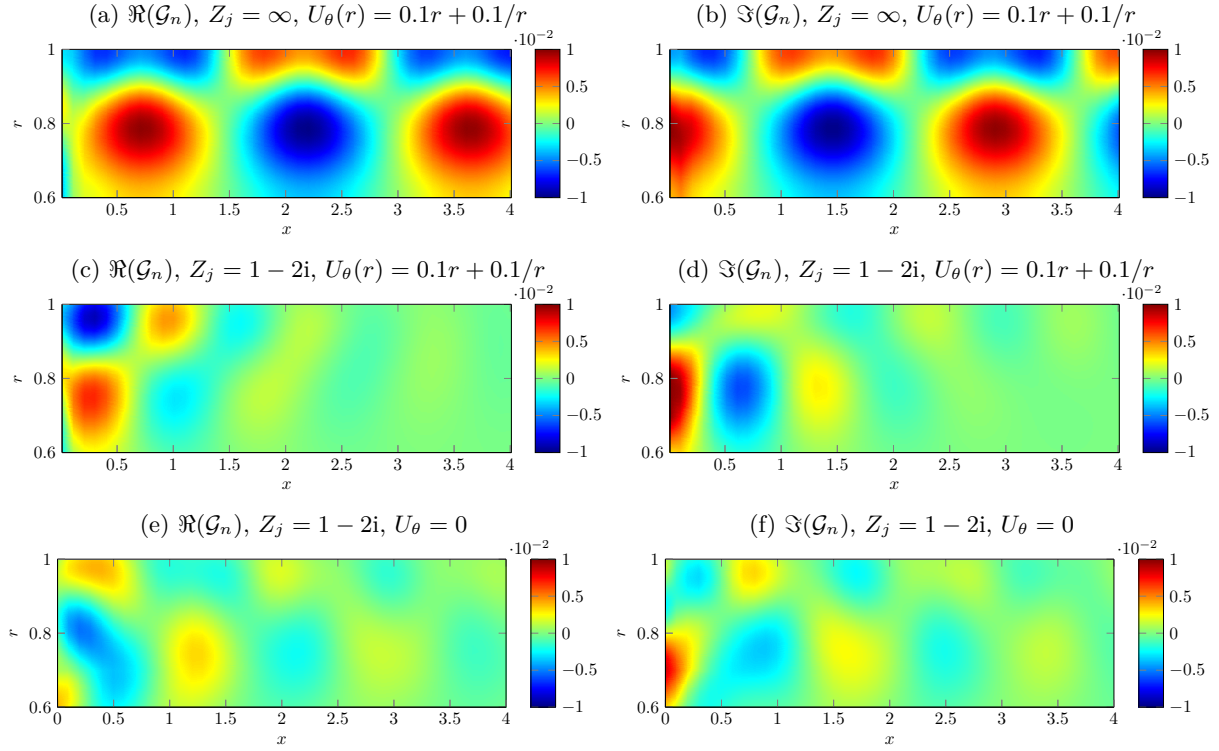


Figure 9: Colour plot of the asymptotic Green's function with a source at  $(x_0, r_0) = (0, 0.8)$  as  $x$  and  $r$  vary. Top: simple test case with hard walls. Middle: simple test case with lined walls. Bottom: simple test case with lined walls and no swirl, reproduced from Mathews<sup>3</sup>

In Figures 9e and 9f we have plotted the Green's function for the simple test case with lining, but in the case when we have no swirl so  $U_\theta = 0$ . This is reproduced from Mathews.<sup>3</sup> We can see that this differs significantly from Figures 9c and 9d, showing how important it is to model the swirl accurately.

## VI. Effect of entropy on the Green's function

In Mathews<sup>3</sup> we saw that when we had a base flow varying in entropy there are various effects on the eigenmodes, with one of them being that the number of cut-on eigenmodes varies with entropy. Since the acoustic contribution from the Green's function primarily comes from the cut-on modes, this will see the Green's function change significantly as we vary entropy.

In Figure 10 we have plotted the contribution towards the Green's function from the three furthest upstream cut-on eigenmodes as the entropy varies. The base flow entropy is given by  $S_0(r) = -\log(r^\beta)$ , which comes from Cooper.<sup>26</sup> We investigate this entropy with  $\beta = -0.3$  (left),  $\beta = 0$  (middle) and  $\beta = 0.3$  (right). As we vary the value of  $\beta$ , the density, speed of sound and pressure of the base flow all vary since the base flow must satisfy the Euler equations. This then causes functions such as  $q_n(r, \kappa)$ ,  $\Phi(r, \kappa)$  to vary with entropy.

In Figure 10 we give the asymptotic eigenmode in bold and the numerical eigenmode in *italic*. The asymptotic Green's function is given by solid lines and the numerical Green's function by dashed lines, with red and blue corresponding to the real and imaginary parts. Subsequent upstream modes for all three values of  $\beta$  are cut-off, with the contribution to the Green's function from these modes several orders of magnitude smaller than the contribution from the dominant cut-on modes. In Figure 10 we can see that for all values of entropy our asymptotic Green's function is very accurate compared to the numerical Green's function.

We can see in Figure 10 that the contribution to the Green's function from the furthest upstream eigenmode (top row) is very similar for all values of  $\beta$ . When we consider the next eigenmode (second row) we can see that the Green's function changes significantly as we vary the entropy. For example, the

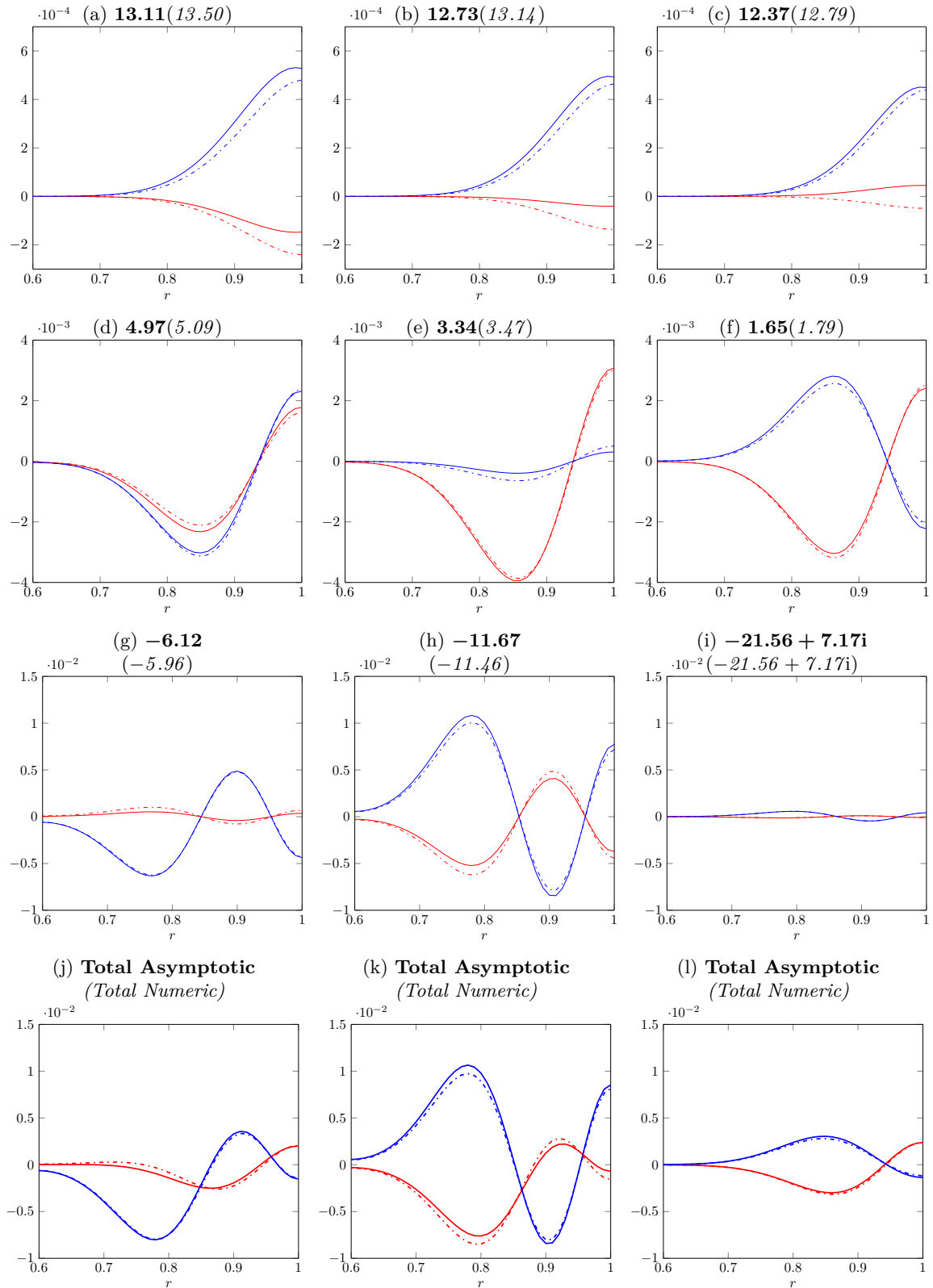


Figure 10: **Real and imaginary parts of asymptotic and numerical Green's function as entropy varies.** Parameters are  $U_x(r) = 0.3 + 0.2r^2$ ,  $U_\theta(r) = 0.1r + 0.1/r$ ,  $n = 32$ ,  $\omega = 50$ ,  $h = 0.6$  and hard walls.

We have set  $x - x_0 = 0.5$  and  $r_0 = 0.8$ . The entropy is  $\mathcal{S}_0(r) = -\log(r^\beta)$  with  $\beta = -0.3$  (left),  $\beta = 0$  (middle) and  $\beta = 0.3$  (right).

From top to bottom we have plotted the Green's function from the three most cut-on upstream acoustic modes and at the bottom the sum of these Green's functions. *Numerical eigenmodes are italic*, **asymptotic eigenmodes are bold**. Solid lines are the asymptotic Green's function, dashed lines are the numerical Green's function. Red is for real, blue is for imaginary part.

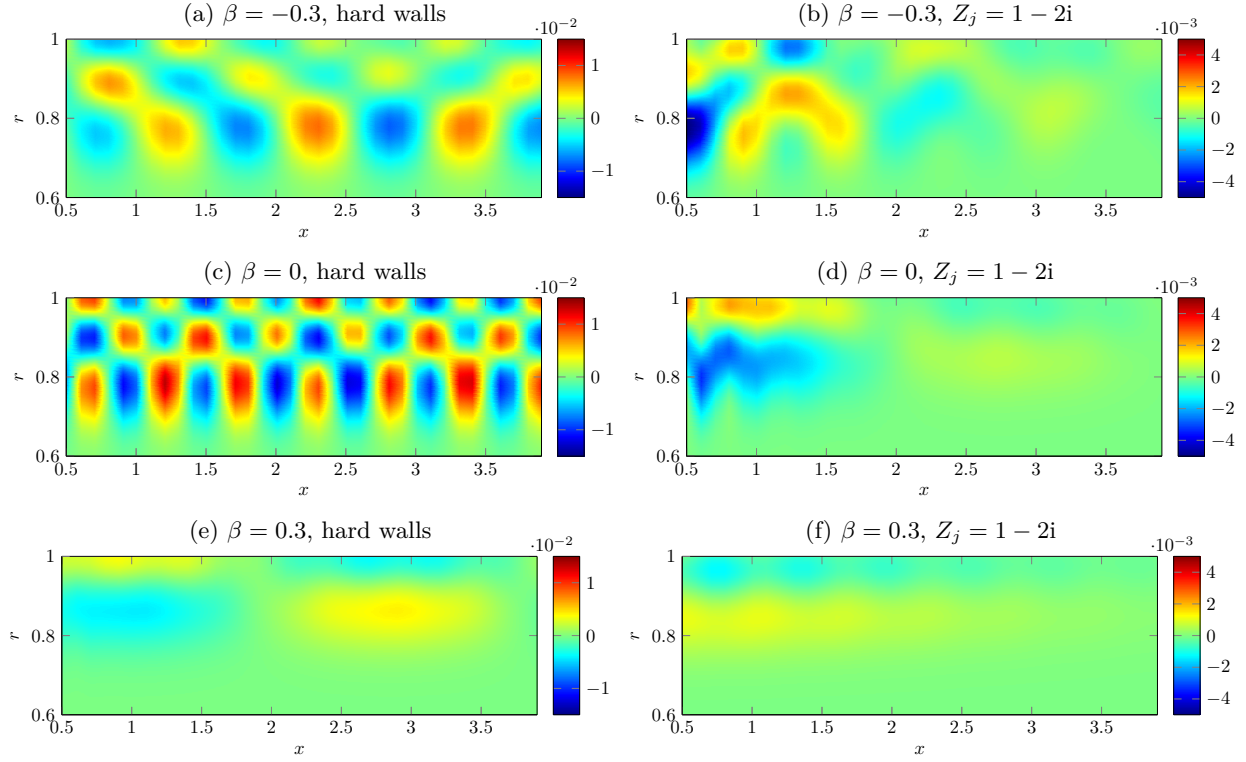


Figure 11: Colour plot of real part of asymptotic Green's function with a source at  $(x_0, r_0) = (0, 0.8)$  as  $x$  and  $r$  vary. The parameters are the same as Figure 10. From top to bottom we consider  $\beta = -0.3$ ,  $\beta = 0$  and  $\beta = 0.3$ . On the left is the Green's function in hard-walled duct and on the right a lined duct with impedance  $Z_j = 1 - 2i$ .

imaginary part of the Green's function is mostly negative when  $\beta = -0.3$ , close to zero when  $\beta = 0$  and mostly positive when  $\beta = 0.3$ . The differences in the Green's function are because the eigenmode has moved a significant amount as we have varied the entropy.

When we consider the contribution to the Green's function from the third furthest upstream cut-on eigenmode (third row), we can see significantly different shapes and amplitudes for the Green's function. When  $\beta = 0.3$  this eigenmode is cut-off with imaginary part 7.17, while when  $\beta = 0$  or  $\beta = -0.3$  it is completely cut-on. Finally, in the fourth row we see the total acoustic contribution, obtained by summing the contribution from the three most cut-on modes, with vastly different Green's functions as the entropy varies. We note that when  $\beta = 0$  and  $\beta = -0.3$  the third eigenmode contributes most to the Green's function, since it  $\mathcal{O}(10^{-2})$ . However, when  $\beta = 0.3$  the second mode is the dominant eigenmode. Thus the addition of entropy not only changes the Green's function at each mode, but changes the dominant eigenmode(s).

In Figure 11 we show the real part of the total asymptotic Green's function for a source at  $(x_0, r_0) = (0, 0.8)$  as  $x$  and  $r$  vary. We can see the effect of both entropy and lining on the Green's function. We notice that in both a lined duct and a hard-walled duct when  $\beta = 0.3$  the Green's function is a lot smaller in magnitude than when  $\beta = 0$  or  $\beta = -0.3$ .

We can very visibly see that the Green's function is very different for the three values of entropy. As the entropy varies, we can see that we have three completely different patterns, and the period of the patterns in the axial direction changes massively for both hard and lined duct walls.

When we add lining we find the Green's function decays in the axial direction for all values of entropy. We also find that in a lined duct the Green's function has a significantly smaller magnitude than in a hard-walled duct, with the right hand scale in Figure 11 three times smaller than the scale on the left. Again, we see completely different patterns in the Green's function as we vary the entropy.

It is clear from our results that a small difference in entropy can modify the Green's function substantially and thus we need to model the base flow entropy correctly to accurately calculate the Green's function.

## VII. Green's function for realistic mean flow

We next consider the Green's function for realistic mean flow in an aeroengine. We consider shear and swirl profiles which are based upon CFD calculations between the rotor and stator. This brings about a problem, since in realistic CFD calculations the shear and the swirl have boundary layers close to the duct walls due to viscosity. This will cause problems with the asymptotics, since when we consider the asymptotic method we need to go slightly outside the duct, in which case both the shear and the swirl would then be negative. We firstly investigate the effect of the boundary layer numerically, and show that we can get good Green's function approximations by ignoring the boundary layer.

### A. Effect of boundary layer

In Figure 12 we consider a realistic shear and swirl profile at low speed with and without a boundary layer. The mean flow profiles are plotted in green in Figure 12. We have then created a boundary layer by subtracting off an exponential function at both duct walls, and this is plotted in orange in Figure 12. In practice, we would have to perform the calculation the other way round, and remove the boundary layer rather than add it. One possible method for this would be to use least-squares and assume the boundary layer is some exponential profile.

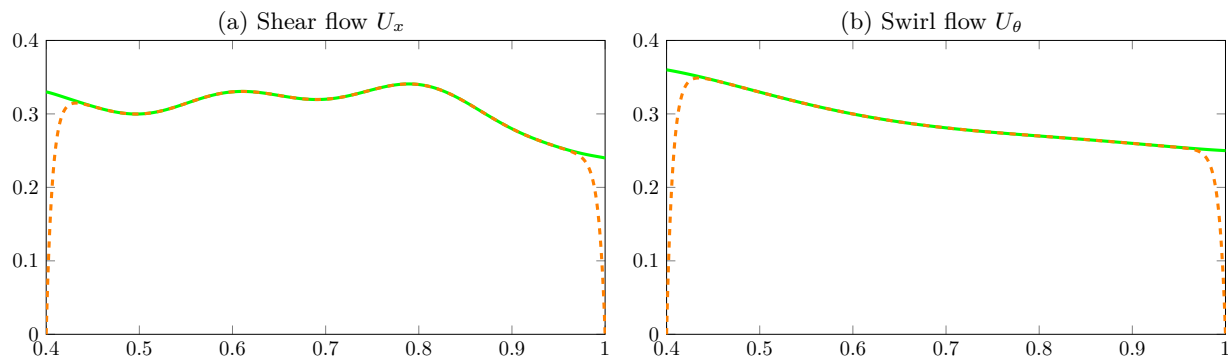


Figure 12: Plot of realistic shear and swirl flow at low speed. In orange (dashed) is the flow with a boundary layer and in green (solid) is the flow without a boundary layer.

#### 1. Hard walls

In Figure 13 we compare the Green's function for the two difference mean flow profiles for a hard-walled duct. In solid lines we have the Green's function for the mean flow with no boundary layer, while dashed lines correspond to the Green's function when the mean flow has a boundary layer. We have plotted the real part of the Green's function in red and the imaginary part in blue for each eigenmode.

Overall, we can see the Green's function changes by a small amount with the introduction of a boundary layer, but the difference is small enough that it can be neglected. In Figures 13b, 13c and 13e we can see that both the eigenmode and Green's function are largely unaffected by the introduction of the boundary layer. In Figures 13a and 13d the effect is more noticeable, since the eigenmodes have changed by a larger amount. The differences in the Green's function for these modes due to the boundary layer then give a small difference in the total Green's function in Figure 13f. We have not considered the contribution from the critical layer, although when we have a boundary layer the right edge of the critical layer is now at infinity.

#### 2. Lined walls

We also consider the effect of the boundary layer when we have acoustic lining on the duct walls. The Ingard-Myers boundary condition is designed so that we do not have to consider the boundary layer for a flow in the duct. Thus, if the Ingard-Myers boundary condition is a good approximation then our Green's function shouldn't change too much. In Figure 14 we see exactly that. We have calculated the Green's function for the mean flow with and without a boundary layer, and applied the same Ingard-Myers boundary condition for both flows.

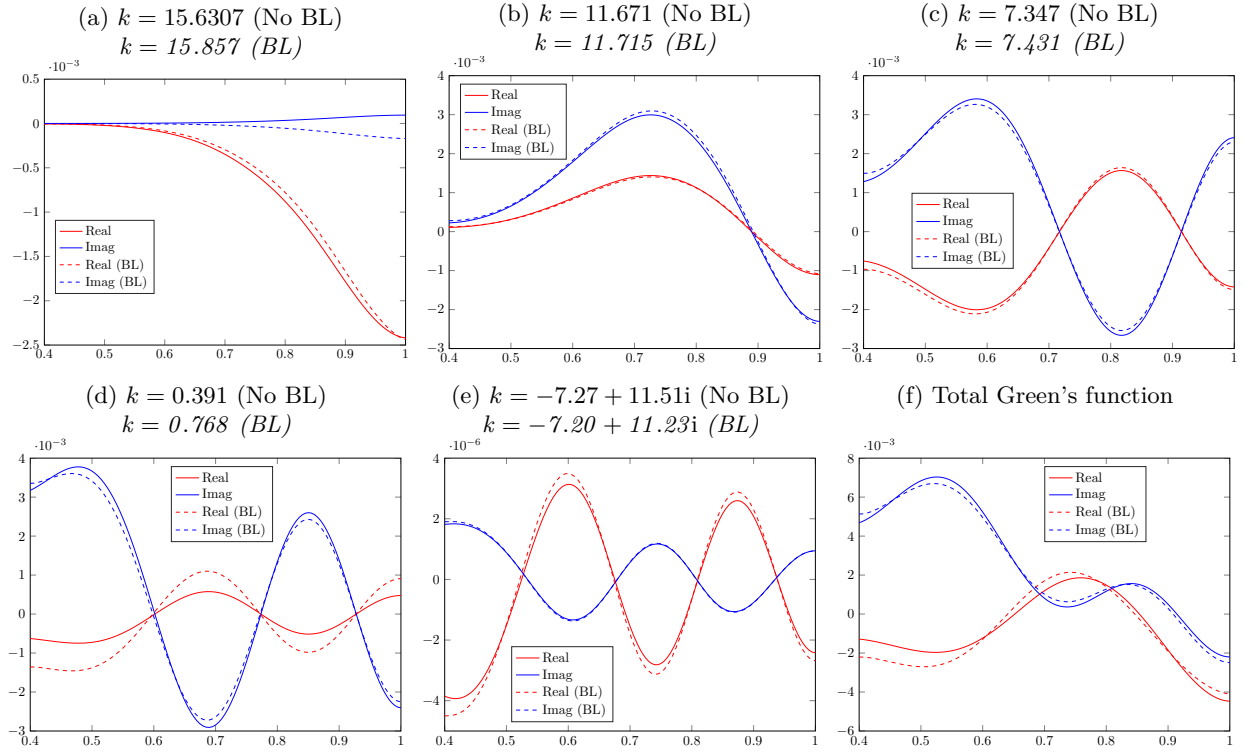


Figure 13: Comparison of numerical Green's function for a mean flow with and without a boundary layer in a duct with hard walls. Source is  $r_0 = 0.8$  and  $x - x_0 = 0.5$ . The other parameters are  $\omega = 25$  and  $n = 8$ .

We can see that introducing the boundary layer directly into the flow rather than through the Ingard-Myers boundary condition does not have much of an effect on the total Green's function in Figure 14f. It is really only the Green's function from the eigenmode in Figure 14d which differs with the introduction of a boundary layer, with the Green's function in Figures 14a, 14b, 14c and 14d very similar. We can conclude that neglecting the boundary layer will generally still give us very good agreement for the Green's function, and will allow us to use our asymptotic method to calculate the Green's function.

## B. Realistic mean flow at low speed

We consider the shear and swirl profile given in Figure 12 but without a boundary layer. This is representative of the mean flow in an aeroengine at low speed. We consider a slightly different regime where  $\omega = 22$  and  $n = 7$ , and we consider both hard and lined walls. We firstly consider the eigenmodes, which are shown in Figure 15. With this more complicated mean flow profile, we are very likely to find regions of  $\kappa$  space where  $q_n$  has two or more zeros close to the duct. In these regions the asymptotic method fails, mainly because there currently is no uniformly-valid formula like Langer's for two turning points. Even in the case we have chosen one of the downstream cut-on modes lies in this two turning point region.

### 1. Eigenmodes for a hard-walled duct

As mentioned above, we do not find all of the asymptotic cut-on modes in Figure 15. This is because the furthest downstream cut-on mode lies in a region where  $q_n(r, \kappa)$  has two zeros close to the duct. This region is shaded in red in Figure 15d.

We can see clearly that despite the more complicated shear and swirl profiles we approximate all the other numerical modes accurately. The accuracy is very comparable to the previous example for an analytical mean flow in Figure 6. For example, the fifth asymptotic cut-off mode has a relative error of 0.28% compared to the numerical eigenmode.



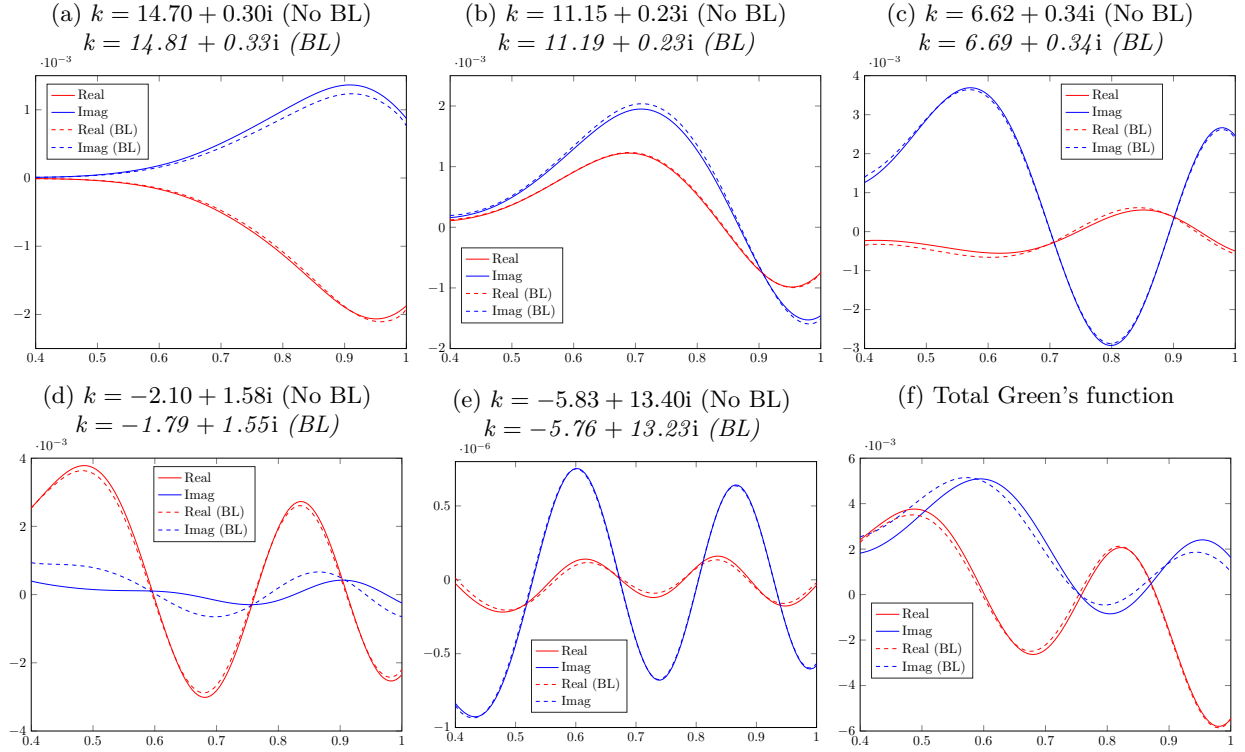


Figure 14: Comparison of numerical Green's function for a mean flow with and without a boundary layer in a duct with lined walls of impedance  $Z_j = 1 - 2i$ . Source is at  $r_0 = 0.8$  and  $x - x_0 = 0.5$ . The other parameters are  $\omega = 25$  and  $n = 8$ .

## 2. Eigenmodes for an acoustically lined duct

In a lined duct we again fail to find the furthest downstream cut-on mode since the mode still lies in the two turning point region. We are able to find the furthest upstream cut-on mode, despite it being very close to the edge of the  $\mathcal{K}$  region.

We find the cut-off modes are well approximated, although we solve the zero turning point dispersion relation for the two cut-off modes with the smallest imaginary part. As we expect, the introduction of lining shifts the cut-off modes to the right, and breaks the symmetry of the cut-off modes. It is interesting to note that the furthest upstream cut-on mode has a larger imaginary part than the next cut-on mode, which is something we were not expecting.

## 3. Green's function for a hard-walled duct

We consider the contribution to the Green's function from the three cut-on modes and the first two upstream cut-off modes in Figure 16. The first of these cut-off modes only has a small imaginary part so the Green's function contribution from the mode  $k = -6.37 + 2.97i$  in Figure 16d is of a similar magnitude to the cut-on modes in Figures 16a, 16b and 16c. In fact, the three cut-on modes and first cut-off modes all have magnitude  $\mathcal{O}(10^{-3})$ , and they will all contribute towards the total Green's function and there is no single dominant eigenmode. The contribution to the Green's function from the second cut-off mode,  $k = -6.47 + 13.82i$ , is  $\mathcal{O}(10^{-7})$  so it is insignificant compared to the other modes. The accuracy of the asymptotic approximations for each mode is very good and compares extremely favourably to the numerical results. For a couple of modes the amplitude of the asymptotic Green's function is not perfect, such as in Figure 16e. This is because the mode is quite close to the edge of the  $\mathcal{K}$  region.

## 4. Green's function for an acoustically lined duct

We also calculate the Green's function when we have lined duct walls in Figure 17. The first thing we note is that the accuracy of the asymptotic Green's function is very good compared to the numerical results. Only



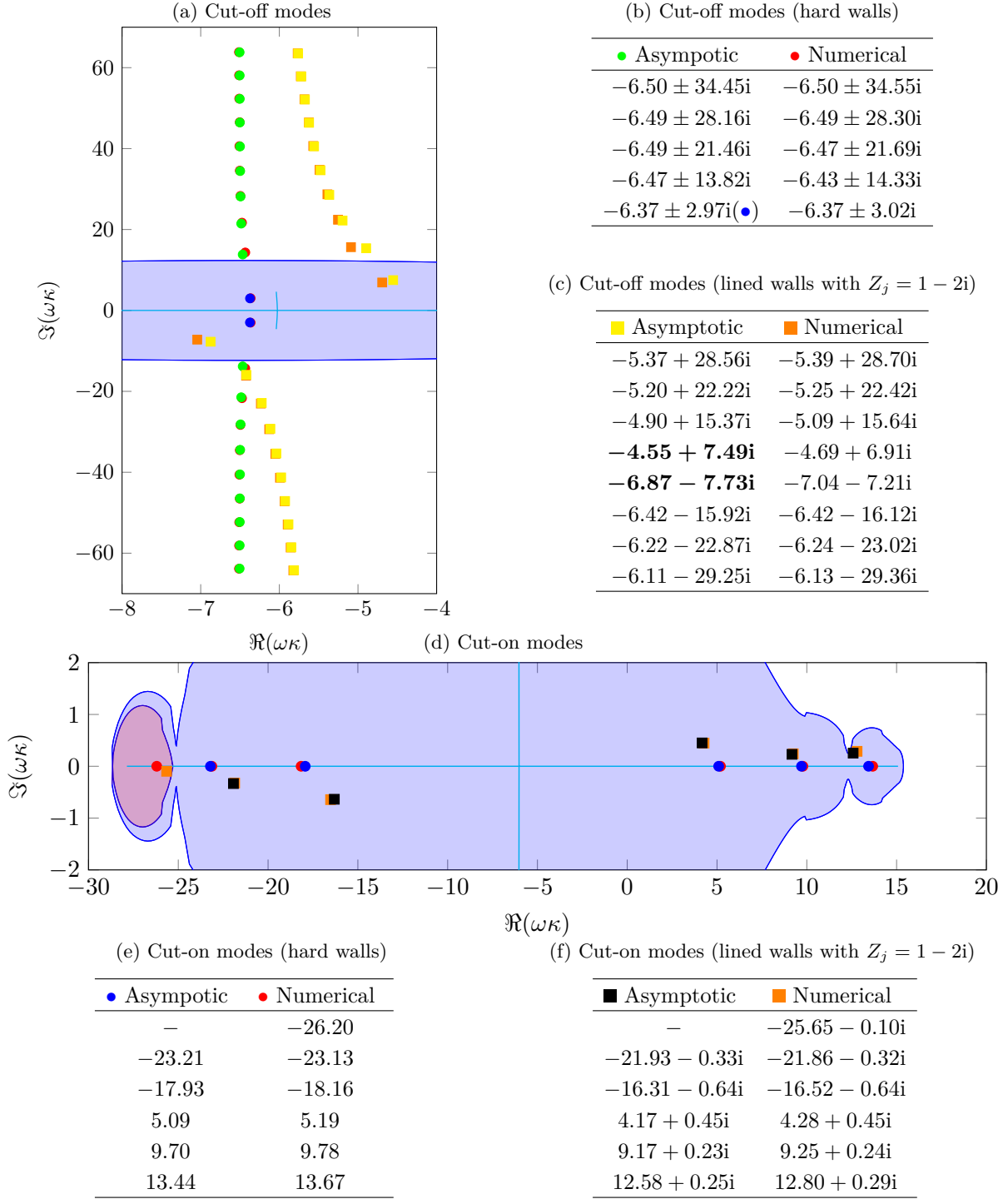


Figure 15: **Realistic mean flow at low speed.** Plot of the asymptotic and numerical eigenmodes. The parameters were  $\omega = 22$ ,  $n = 7$ , with both hard walls and lined walls of impedance  $Z_j = 1 - 2i$ .

in Figure 17d is the asymptotic Green's function a poor approximation. Even so, it has roughly the correct shape and it is just the amplitude that is wrong. This poor approximation stems from the fact that the eigenmode  $k = -4.55 + 7.49i$  is in the region  $\mathcal{K}$  but we have used the zero turning point dispersion relation since it is more accurate.

Unlike when we had hard walls, the contribution from the first cut-off mode in Figure 17d is one order of magnitude smaller than the contributions from the cut-on modes. The contribution from the second cut-off mode in Figure 17e is again  $\mathcal{O}(10^{-7})$ , and all subsequent cut-off modes have even smaller contributions.

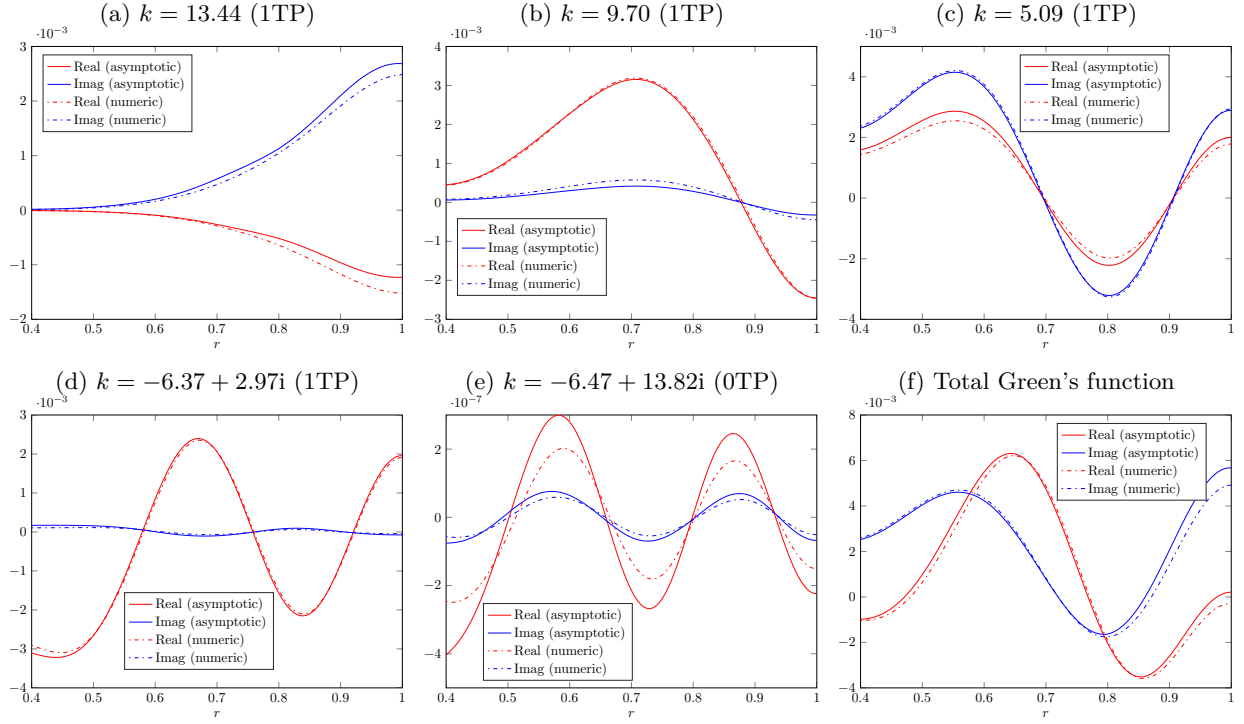


Figure 16: Comparison of the asymptotic and numerical Green's function for realistic mean flow at low speed in a hard-walled duct. We have set  $r_0 = 0.8$  and  $x - x_0 = 0.5$ , and additionally  $\omega = 22$  and  $n = 7$ .

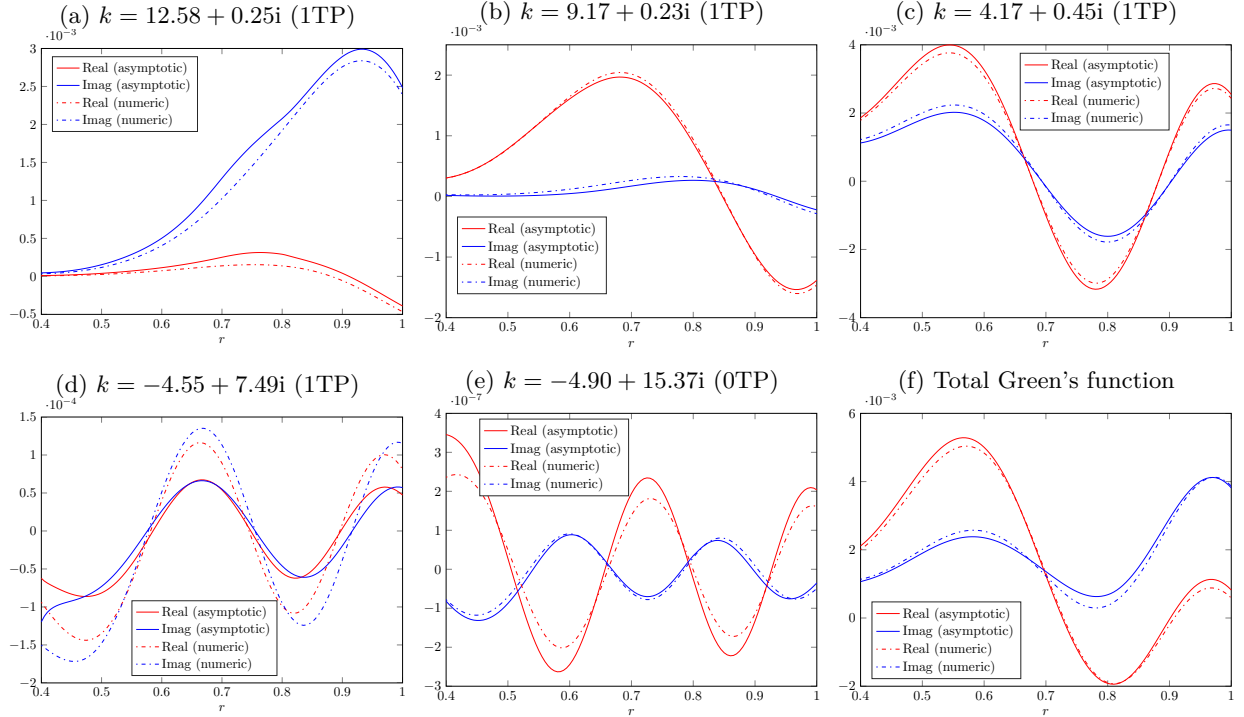


Figure 17: Comparison of the asymptotic and numerical Green's function for realistic mean flow at low speed in an acoustically lined duct. We have set  $r_0 = 0.8$  and  $x - x_0 = 0.5$  and additionally  $\omega = 22$  and  $n = 7$ .

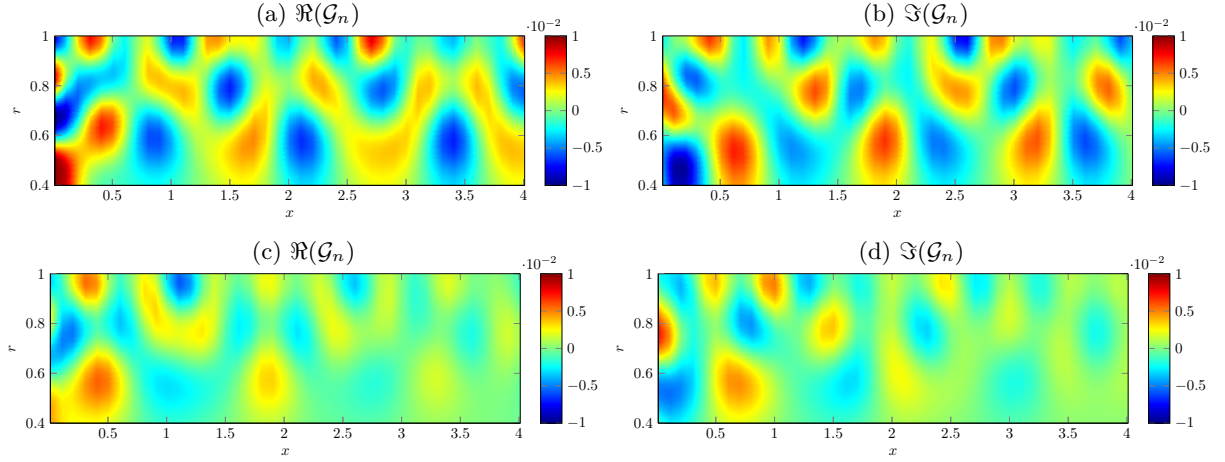


Figure 18: Colour plot of the real and imaginary parts of the asymptotic Green's function for hard walls (top) and lined walls (bottom). The source is at  $(x_0, r_0) = (0, 0.8)$  and we let  $x$  and  $r$  vary.

Thus the total Green's function really only depends on the three cut-on modes.

In Figure 18 we show colour plots of the real and imaginary parts of the asymptotic Green's function for the realistic mean flow at low speed. We have considered a point source at  $(x_0, r_0) = (0, 0.8)$  and varied  $x$  and  $r$ . We can clearly see the effect of the lining. The presence of lining changes the axial periodic and magnitude of the Green's function, as well as ensuring it decays in the axial direction.

### C. Realistic shear and swirl at high speed

Finally, we consider realistic shear and swirl at high speed, with the mean flow profiles given in Figure 19. We have ignored the boundary layers since we saw in Section VII.A their effect was minimal. We consider a

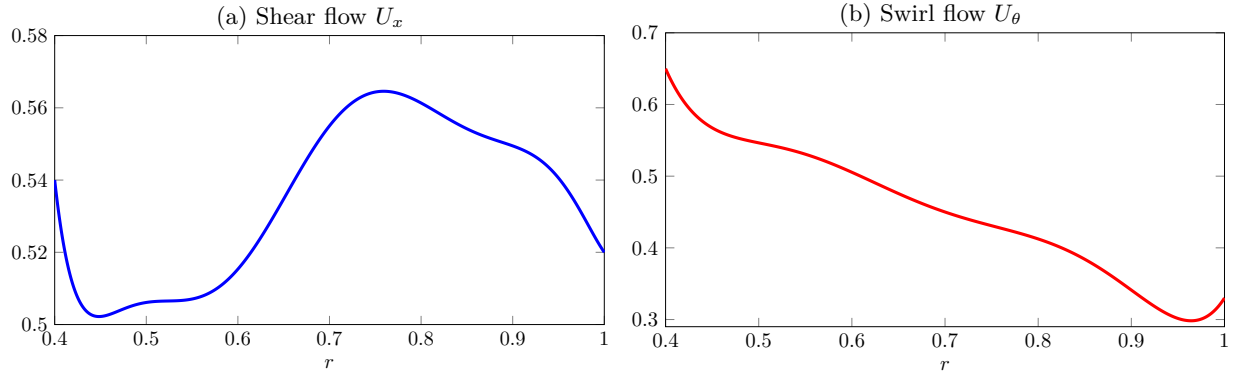


Figure 19: Plot of realistic shear and swirl flow at high speed.

frequency of  $\omega = 19.5$ , which corresponds to roughly 1600Hz. We only plot the Green's function for a lined duct, with impedance at both duct walls of  $Z_j = 1 - 2i$ .

In Figure 21 we plot the Green's function for each upstream mode, with a source at  $r_0 = 0.8$  and  $x - x_0 = 0.5$ . We have chosen the azimuthal number  $n = 8$ . We can see that we get excellent agreement between the asymptotic and numerical Green's function for each and every eigenmode. In this case we have only two cut-on modes and the Green's function associated to these modes are of a similar magnitude. The contribution to the Green's function from the cut-off modes is several orders of magnitude smaller than that from the cut-on modes.

The final thing we do is to consider the Green's function as we vary both  $x$  and  $r$  for a single source point at  $(x_0, r_0) = (0, 0.8)$ . We compare the asymptotic Green's function to the numerical Green's function in Figure 21. We can see that the asymptotic results agree extremely favourably with the numerical results.

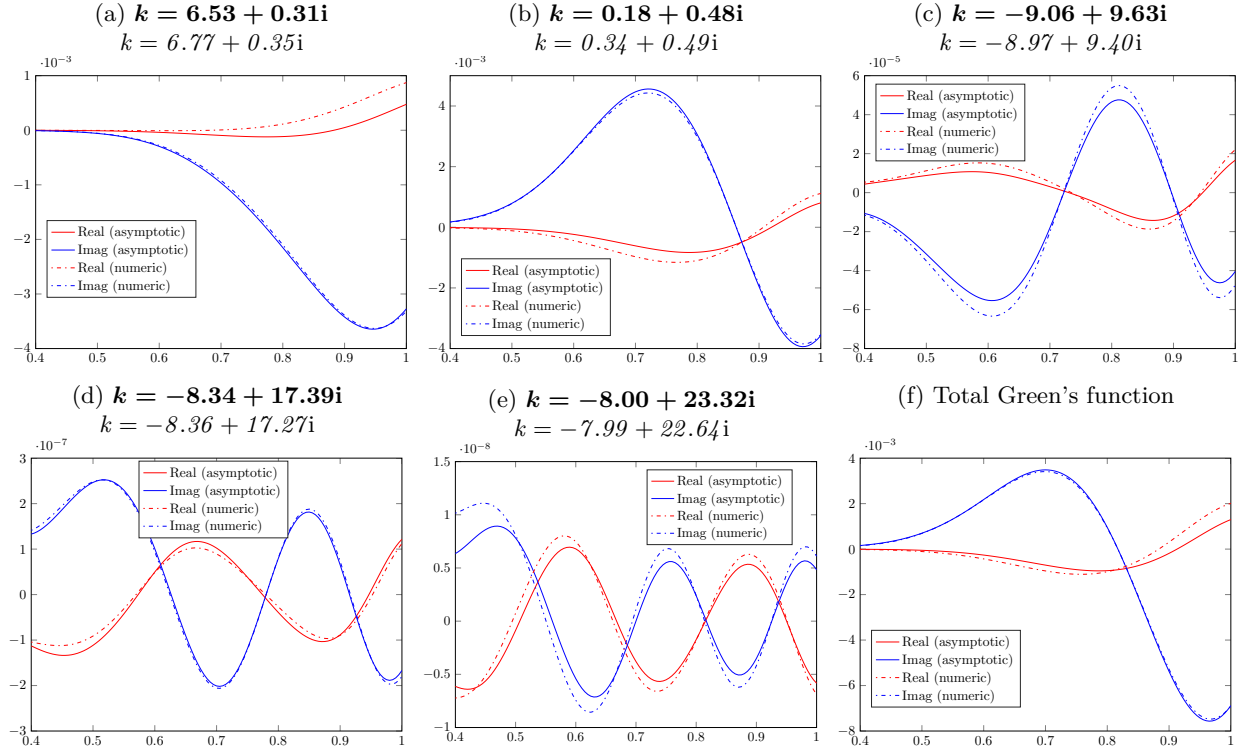


Figure 20: Comparison of the asymptotic and numerical Green's function for realistic mean flow at high speed in an acoustically lined duct. We have set  $r_0 = 0.8$  and  $x - x_0 = 0.5$ , with  $\omega = 19.5$  and  $n = 8$ . The asymptotic Green's function is the solid line and the asymptotic eigenmodes are in bold. The numerical Green's function is the dashed line and the numerical eigenmodes are italic.

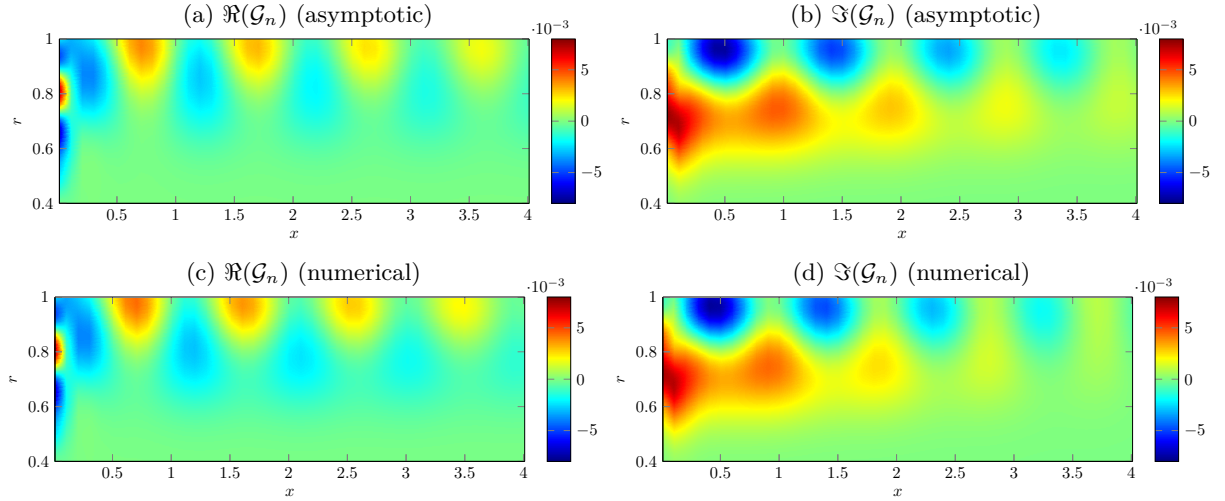


Figure 21: Colour plot of the real and imaginary part of the asymptotic Green's function (top) and numerical Green's function (bottom). We have set  $r_0 = 0.8$  and  $x_0 = 0$ . The other parameters are  $n = 8$ ,  $\omega = 19.5$ ,  $Z_j = 1 - 2i$  and shear and swirl profiles given in Figure 19.

## VIII. Conclusion

We have shown that we can accurately calculate the Green's function analytically for any shear and swirl profiles with only radial dependence. Additionally, we can find an analytical expression for the eigenmodes, although it has to be solved numerically. It remains to sum the Green's function  $G_n$  for each azimuthal wavenumber  $n$ . Our results will be extremely useful, namely in the beamforming technique described in Section III.

We have already considered the effect of a base flow with varying entropy on the asymptotic and numerical Green's function. In Mathews<sup>3</sup> we also consider the effect of entropy on the asymptotic and numerical eigenmodes. Future work on this topic involves looking at lining and/or ducts which vary axially or circumferentially. A method for finding the Green's function in the case of lining varying circumferentially is given in Mathews.<sup>3</sup>

Another source of future work would be to come up with an accurate, fast way of evaluating the contribution from the integral around the critical layer. Although we believe this can be ignored in most cases, there will be some cases where it needs to be considered.

## Acknowledgements

This work was supported by the UK Engineering and Physical Sciences Research Council (EPSRC) grant EP/H023348/1 for the University of Cambridge Centre for Doctoral Training, the Cambridge Centre for Analysis.

The authors would also like to thank Rolls-Royce for the provision of the CFD fan data to allow the Green's function to be tested in realistic mean flow. Rolls-Royce also provided support in using the data.

## References

- <sup>1</sup>Posson, H. and Peake, N., "The acoustic analogy in an annular duct with swirling mean flow," *Journal of Fluid Mechanics*, Vol. 726, 6 2013, pp. 439–475.
- <sup>2</sup>Bender, C. M. and Orszag, S. A., *Advanced mathematical methods for scientists and engineers I: Asymptotic methods and perturbation theory*, Vol. 1, Springer, 1978.
- <sup>3</sup>Mathews, J. R., *Mathematical modelling of noise generation in and propagation through turbomachinery*, Ph.D. thesis, University of Cambridge, 2016.
- <sup>4</sup>Wundrow, D. W. and Khavaran, A., "On the applicability of high-frequency approximations to Lilley's equation," *Journal of Sound and Vibration*, Vol. 272, No. 3, 2004, pp. 793–830.
- <sup>5</sup>Cooper, A. J. and Peake, N., "Upstream-radiated rotor-stator interaction noise in mean swirling flow," *Journal of Fluid Mechanics*, Vol. 523, 2005, pp. 219–250.
- <sup>6</sup>Heaton, C. J. and Peake, N., "Acoustic scattering in a duct with mean swirling flow," *Journal of Fluid Mechanics*, Vol. 540, 2005, pp. 189–220.
- <sup>7</sup>Vilenski, G. G. and Rienstra, S. W., "On hydrodynamic and acoustic modes in a ducted shear flow with wall lining," *Journal of Fluid Mechanics*, Vol. 583, No. 4, 2007, pp. 45–70.
- <sup>8</sup>Vilenski, G. G. and Rienstra, S. W., "Numerical study of acoustic modes in ducted shear flow," *Journal of Sound and Vibration*, Vol. 307, No. 3, 2007, pp. 610–626.
- <sup>9</sup>Posson, H. and Peake, N., "Acoustic analogy in swirling mean flow applied to predict rotor trailing-edge noise," *18th AIAA/CEAS Aeroacoustics Conference, Colorado Springs*, Vol. 2267, 2012.
- <sup>10</sup>Posson, H. and Peake, N., "Swirling mean flow effect on fan-trailing edge broadband noise in a lined annular duct," *19th AIAA/CEAS Aeroacoustics Conference, Berlin*, Vol. 2150, 2013.
- <sup>11</sup>Ingard, U., "Influence of fluid motion past a plane boundary on sound reflection, absorption, and transmission," *The Journal of the Acoustical Society of America*, Vol. 31, No. 7, 1959, pp. 1035–1036.
- <sup>12</sup>Myers, M., "On the acoustic boundary condition in the presence of flow," *Journal of Sound and Vibration*, Vol. 71, No. 3, 1980, pp. 429–434.
- <sup>13</sup>Posson, H., Moreau, S., and Roger, M., "Broadband noise prediction of fan outlet guide vane using a cascade response function," *Journal of Sound and Vibration*, Vol. 330, No. 25, 2011, pp. 6153–6183.
- <sup>14</sup>Sijtsma, P., "Using phased array beamforming to locate broadband noise sources inside a turbofan engine," *AARC Engine Noise Phased Array Workshop, Cambridge, MA, USA*, 2006.
- <sup>15</sup>Sijtsma, P., "Feasibility of in-duct beamforming," *13th AIAA/CEAS Aeroacoustics Conference, AIAA*, Vol. 3696, 2007.
- <sup>16</sup>Pires, L. S., Dougherty, R. P., Gerges, S. N., and Catalano, F., "Predicting Turbulent Decorrelation in Acoustic Phased Array," *50th AIAA Aerospace Sciences Meeting including the New Horizons Forum and Aerospace Exposition*, Vol. 387, 2012.
- <sup>17</sup>Allen, J. B. and Berkley, D. A., "Image method for efficiently simulating small-room acoustics," *The Journal of the Acoustical Society of America*, Vol. 65, No. 4, 1979, pp. 943–950.
- <sup>18</sup>Amiet, R., "Refraction of sound by a shear layer," *Journal of Sound and Vibration*, Vol. 58, No. 4, 1978, pp. 467–482.
- <sup>19</sup>Humphreys, W. M., Hunter, W. W., Meadows, K. R., and Brooks, T. F., "Design and Use of Microphone Directional Arrays for Aeroacoustic Measurements," *AIAA Paper 98-0471, 36th Aerospace Sciences Meeting & Exhibit, Reno NV*, Citeseer, 1998.
- <sup>20</sup>Padois, T., Prax, C., and Valeau, V., "Traitement d'antenne appliqué aux mesures en soufflerie: Prise en compte des effets de l'écoulement sur la propagation au moyen d'un modèle numérique," *10ème Congrès Français d'Acoustique*, 2010.
- <sup>21</sup>Sijtsma, P., "Green's functions for in-duct beamforming applications," *18th AIAA/CEAS Aeroacoustics Conference, AIAA*, Vol. 2248, 2012.
- <sup>22</sup>Fleury, V., Mincu, D., and Polacsek, C., "CAA-based acoustic beamforming for noise identification in complex media," *Acoustics 2012*, 2012.

- <sup>23</sup>Brambley, E. J., Darau, M., and Rienstra, S. W., “The critical layer in sheared flow,” *17th AIAA/CEAS Aeroacoustics Conference, Portland*, Vol. 2806, 2011.
- <sup>24</sup>Heaton, C. J. and Peake, N., “Algebraic and exponential instability of inviscid swirling flow,” *Journal of Fluid Mechanics*, Vol. 565, 2006, pp. 279–318.
- <sup>25</sup>Brambley, E. J., “Fundamental problems with the model of uniform flow over acoustic linings,” *Journal of Sound and Vibration*, Vol. 322, No. 4, 2009, pp. 1026–1037.
- <sup>26</sup>Cooper, A. J., “Effect of mean entropy on unsteady disturbance propagation in a slowly varying duct with mean swirling flow,” *Journal of Sound and Vibration*, Vol. 291, No. 3, 2006, pp. 779–801.